IMA Journal of Applied Mathematics (2020) **00**, 1–41
doi:10.1093/imamat/hxaa036

Steady states of thin film droplets on chemically heterogeneous substrates

Weifan Liu*
Department of Mathematics, Syracuse University, Syracuse, New York, 13244, USA
*Corresponding author: wliu07@syr.edu

and

Thomas P. Witelski
Department of Mathematics, Duke University, Durham, North Carolina, 27708-0320, USA

[Received on 1 January 2020; revised on 28 June 2020; accepted on 10 September 2020]

We study steady-state thin films on chemically heterogeneous substrates of finite size, subject to no-flux boundary conditions. Based on the structure of the bifurcation diagram, we classify the 1D steady-state solutions that exist on such substrates into six different branches and develop asymptotic estimates for the steady states on each branch. Using perturbation expansions, we show that leading-order solutions provide good predictions of the steady-state thin films on stepwise-patterned substrates. We show how the analysis in one dimension can be extended to axisymmetric solutions. We also examine the influence of the wettability contrast of the substrate pattern on the linear stability of droplets and the time evolution for dewetting on small domains. Results are also applied to describe 2D droplets on hydrophilic square patches and striped regions used in microfluidic applications.

Keywords: thin films; lubrication theory; heterogeneous substrates; disjoining pressure; pinned droplets.

1. Introduction

Thin liquid films on solid substrates are often seen in nature and engineering applications, e.g. as tear films on the eye, lubricating coatings, and functional layers in microfluidic devices (see, e.g. Thiele *et al.*, 2003). Microfluidic systems manipulate small amounts of fluids, using channels with dimensions at the scale of micrometres (Whitesides, 2006). Microfluidics has found many applications in cell biology and chemical synthesis (Lo, 2013; Whitesides, 2006). The effect of substrate wetting properties on the equilibrium liquid droplet formed on a solid, especially features like contact angle and mass, has attracted extensive research attention due to applications in liquid coating and inkjet printing (Bhushan *et al.*, 2009; Dong *et al.*, 2006; Sakai *et al.*, 2008; Son *et al.*, 2008; Yuan & Lee, 2013). Specifically, the steady-state thin films have been previously studied through the approach of numerical methods, asymptotic approximations and ellipsoidal droplet approximation (Glasner & Witelski, 2003; Gomba & Homsy, 2009; Lubarda & Talke, 2011; Mac Intyre *et al.*, 2016).

Much of the theoretical understanding of thin films has been limited to films on homogeneous substrates. Profiles of steady-state solutions under the action of different forms of intermolecular potentials of homogeneous substrates have been previously investigated and described (Bertozzi *et al.*, 2001; Glasner & Witelski, 2003; Gomba & Homsy, 2009). In one study, Glasner & Witelski (2003) considered an isolated steady-state droplet parametrized by uniform pressure on an infinite domain, given by the homoclinic solution of the system. Through asymptotic matching, they showed that at leading order, large homoclinic droplets could be well approximated by parabolic profiles. In another study, Bertozzi *et al.* (2001) performed similar analysis and computations for steady-state thin films on

finite domains. Asymptotic analysis for both the bifurcation structure and the solution profile of such films were presented.

However, many naturally occurring surfaces are chemically heterogeneous due to contamination or differentiated structures in biological or other contexts. Tailored chemically heterogeneous substrates have been increasingly used for the engineering of micropatterns of thin films and applications that require accurate dispensing and distribution of liquids on solid surfaces (Zope *et al.*, 2001). One example of such applications is in the design of the chemical patterns of the nozzle plate in inkjet print heads (Bliznyuk, 2011; Kooij *et al.*, 2012). Quantifying the characteristics of wetting layer on the nozzle plate and designing suitable chemical patterns to control the motion of the ink are critical to improve the printing quality (Bliznyuk, 2011; Kooij *et al.*, 2012). Another application is microcontact printing where a stamp is used to transfer the material onto a substrate to create a desired pattern. Understanding equilibrium droplet shapes on chemically patterned substrates is essential to optime the printing process (Darhuber *et al.*, 2000). Chemically patterned substrates have also been used in the fabrication of polymer field effect transistors where a substrate with a hydrophobic stripe is employed to split a deposited liquid droplet (Wang *et al.*, 2004).

Previously, Lenz & Lipowsky (1998) investigated the morphologies of different equilibrium states of liquids on a surface that consists of hydrophilic domains in a hydrophobic matrix. By minimizing the interfacial free energy subject to constant liquid volume, they found that the different morphologies are determined by the liquid volume and the area fraction of the hydrophilic domains. Kašpar *et al.* (2016) explored the effect of alternating hydrophobic and hydrophilic areas of a rectangular micro-arrayed surface on the overall confinement and spillover of water droplets. They gave an estimate for the contact angle of the droplet in terms of the height of the spherical cap h and a coefficient a that accounts for the properties of the confining surface.

In the limit of low Reynolds number, the governing equations for a slowly varying free surface flow of a viscous liquid coating a solid surface can be reduced to an evolution equation for the film thickness; see, e.g. Ockendon & Ockendon (1995). The lubrication model describing film flow subject to strong surface tension effects on a homogeneous partially wetting solid substrate is a fourth-order non-linear parabolic differential equation (Craster & Matar, 2009; Myers, 1998; Oron *et al.*, 1997), written here for 1D problems,

$$\frac{\partial h}{\partial t} = \frac{\partial}{\partial x}\left(h^3 \frac{\partial}{\partial x}\left[\tilde{\Pi}(h) - \frac{\partial^2 h}{\partial x^2}\right]\right), \tag{1.1}$$

where $h(x,t)$ is the thickness of the film, x is the coordinate in the direction of flow and t is the time. Here, we will consider only the simple form $\tilde{\Pi} = A\Pi(h)$ where A is the Hamaker constant and $\Pi(h)$ is the homogeneous disjoining pressure function which characterizes the wetting properties of the fluid on the substrate. The form of the disjoining pressure function $\Pi(h)$ we will use is described in Section 2. The Hamaker constant A determines the equilibrium contact angle for steady liquid droplets on the substrate (see, e.g. Brasjen & Darhuber, 2011). Numerical simulations of similar lubrication models have been presented in Kargupta *et al.* (2000) and Kargupta & Sharma (2001, 2002) to inspire experimental studies and illustrate the instability and pattern formation of thin film on chemically heterogeneous substrates with a stepwise pattern. More systematic analytical studies using lubrication approximation were presented in Brusch *et al.* (2002), Kao *et al.* (2006) and Thiele *et al.* (2003) where a spatially dependent Hamaker coefficient $A(x)$ was introduced in the long-wave equation. A disjoining pressure of the form

$$\tilde{\Pi}(h,x) = A(x)\Pi(h) \tag{1.2}$$

was used to model thin films on a domain with periodic boundary conditions. Specifically, Brusch *et al.* (2002) and Thiele *et al.* (2003) studied the effect of a smoothly patterned substrate on stationary droplet profiles using wettability as a control parameter. The heterogeneous substrate considered was a small-amplitude sinusoidal modulation of the form $A(x) = 1 + \delta\cos(k_p x)$ where k_p determines the imposed heterogeneity period and $\delta \ll 1$ describes the amplitude of heterogeneity. The smooth spatial variation and the assumption that $\delta \ll 1$ allows for the analysis of the solutions on heterogeneous substrates through an asymptotic expansion in terms of δ. By varying the amplitude and periodicity of the chemical pattern, they identified the parameter range where the pinning mechanism emerges from coarsening.

However, for an engineered patterned substrate, a piecewise constant $A(x)$ would be a better description than a sinusoidal profile. For example, micro-patterned surfaces with alternating relatively hydrophilic and hydrophobic rectangular areas are extensively used in digital microfluidics and high-throughput screening nanoarrays (Kašpar *et al.*, 2016). In such applications, a stepwise Hamaker coefficient is needed to model the chemical properties of the surfaces. Kao *et al.* (2006) studied the stationary states of thin films on substrates with square-wave patterning in both one and two dimensions in addition to those with small-amplitude sinusoidal patterning. Specifically, they considered a piecewise constant $A(x)$ with periodic boundary conditions, given by

$$A(x) = \begin{cases} 1+\delta^3 & \frac{3\pi}{2}n \leqslant k_p x \leqslant \frac{\pi}{2} + \frac{3\pi}{2}n, \\ 1-\delta^3 & \frac{\pi}{2} < k_p x \leqslant \frac{3\pi}{2}, \end{cases} \tag{1.3}$$

for patterning wavenumber k_p and $n = 0, 1$ on $x \in [0, 2\pi]$. To study the bifurcation of stationary states on substrates with such patterning, they wrote $A(x)$ as a Fourier series. In particular, they performed asymptotic analysis for solutions near the bifurcation point. Imperfect bifurcations were observed for the patterning of the form (1.3). They found that the bifurcations and steady states resemble those for sinusoidally patterned substrates. While many papers (including Brasjen & Darhuber, 2011 and Brasjen *et al.*, 2013) have considered thin film models with discontinuous $A(x)$, this formally clashes with the long-wave assumptions used in lubrication theory. However, as described in Lenz & Kumar (2007), good solutions can still be obtained in many cases, though caution should be applied to check their validity.

In this paper, we study the steady-state solutions of thin films on a stepwise-patterned substrate over a range of wettability contrast. We classify the steady-state solutions that exist on such substrates into branches. We find new branches of solutions characterizing pinned droplets that arise as a consequence of the heterogeneity of the substrates. For each branch of solutions, we present systematic asymptotic analysis of the steady-state profile and the structure of the bifurcation diagram. Through asymptotic analysis and numerical simulations, we determine the dependence of steady-state thin films on parameters such as mass, pressure and heterogeneity strength. We employ a phase-plane approach, which allows us to perform asymptotic analysis in the limit of moderate to large heterogeneity contrast. Increasing heterogeneity contrast has an increasing confining and pinning effect on the film droplet, which prevents fluid film from leaking into the more hydrophobic surrounding region. To quantify this phenomenon, we present an effective measure of the fluid leakage and show that the leakage is inversely proportional to the heterogeneity contrast. In addition, we investigate the stability of the steady-state solutions on heterogeneous substrates and show that the analysis derived for 1D solutions can be extended to axisymmetric solutions and more general 2D solutions. Finally, we illustrate the influence of chemical heterogeneity on the dynamics of thin film evolution.

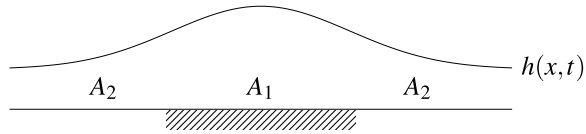

FIG. 1. Schematic diagram of a thin film on a heterogeneous substrate with stepwise chemical patterning yielding relatively hydrophilic (A_1) and hydrophobic ($A_2 > A_1$) regions.

2. Problem formulation

We study 1D thin films on heterogeneous substrates prescribed with a piecewise chemical patterning. Figure 1 shows a schematic diagram of a thin film on a heterogeneous substrate with a relatively hydrophilic region on $-s < x < s$ surrounded by relatively hydrophobic regions on the overall domain $-L \leqslant x \leqslant L$.

Building on the results of Laugesen & Pugh (2000b) that the steady-state solutions of the homogeneous problem (1.1) are periodic functions and are symmetric with respect to local extrema, we will focus on symmetric solutions describing single droplets. Using symmetry reduces the problem to be on the half-domain $0 \leqslant x \leqslant L$ subject to homogeneous Neumann boundary conditions where the lowest-order solutions give height profiles of half-droplets.

We consider a heterogeneous substrate with a stepwise patterning modelled by a piecewise constant function $A(x)$ where the jumps of $A(x)$ need not be small. In particular, we address analysis of steady-state solutions in the limit of moderate to large A_2 relative to A_1 in

$$A(x) = \begin{cases} A_1 & 0 \leqslant x \leqslant s, \\ A_2 & s < x \leqslant L. \end{cases} \tag{2.1}$$

Here, L is the size of the domain, s is the interface of segmentation and A_i are positive constants. For concreteness, we will normalize relative to the hydrophilic region, generally taking $A_1 = 1$ and $A_2 \geqslant A_1$. The schematic diagram in Fig. 1 shows thin film on heterogeneous substrates with such stepwise patterning. Specifically, we consider a disjoining pressure given by a 3–4 inverse power law function which has been used in Schwartz & Eley (1998), Oron & Bankoff (1999, 2001), Glasner & Witelski (2003) and others,

$$\Pi(h) = \frac{\varepsilon^2}{h^3} - \frac{\varepsilon^3}{h^4}, \tag{2.2}$$

and the overall representation of wetting effects is given by $\tilde{\Pi}(h,x) = A(x)\Pi(h)$. The scaling in (2.2) yields a finite limit for the effective contact angle of droplet solutions as $\varepsilon \to 0$; see Glasner & Witelski (2003).

We consider thin films on a finite domain as shown in Fig. 1, subject to no-flux boundary conditions so that the total fluid mass is conserved. Two additional boundary conditions are needed—we impose zero-meniscus (no slope) conditions, $\partial_x h = 0$. These conditions are consistent with uniform film solutions for the homogeneous problem and allow general solutions to be extended to periodic problems (Laugesen & Pugh, 2000a).

As described above, for convenience, we will reduce this to the symmetric problem on the half-domain, $0 \leqslant x \leqslant L$. The evolution of thin films on chemically heterogeneous substrates of finite-length

with chemical patterning $A(x)$ is given by the partial differential equation for the film height $h(x,t)$ (O'Brien & Schwartz, 2002; Oron *et al.*, 1997),

$$\frac{\partial h}{\partial t} = \frac{\partial}{\partial x}\left(h^3 \frac{\partial}{\partial x}\left[\tilde{\Pi}(h,x) - \frac{\partial^2 h}{\partial x^2}\right]\right), \tag{2.3a}$$

subject to the homogeneous Neumann boundary conditions

$$\frac{\partial h}{\partial x}(0,t) = 0, \qquad \frac{\partial^3 h}{\partial x^3}(0,t) = 0, \qquad \frac{\partial h}{\partial x}(L,t) = 0, \qquad \frac{\partial^3 h}{\partial x^3}(L,t) = 0. \tag{2.3b}$$

The conditions at $x = 0$ are symmetry conditions; the conditions at $x = L$, while having the same form, are no-meniscus and no-flux conditions, where the flux is defined as $J(x) \equiv h^3 \partial_x p$ in terms of the pressure

$$p(x,t) \equiv \tilde{\Pi}(h,x) - \frac{\partial^2 h}{\partial x^2} \qquad \text{with} \qquad \tilde{\Pi}(h,x) = A(x)\Pi(h). \tag{2.4}$$

The equivalence with the Neumann conditions can be seen by expanding $J(L) = 0$ using $A'(L) = 0$ and $h(L) > 0$.

This problem has a monotone decreasing energy functional,

$$E = \frac{1}{\bar{A}} \int_0^L A(x)U(h) + \tfrac{1}{2}(\partial_x h)^2 \, \mathrm{d}x \qquad \text{where} \qquad \bar{A} = \frac{1}{L}\int_0^L A(x)\,\mathrm{d}x, \tag{2.5}$$

where $U(h)$ is the potential such that $\frac{dU}{dh} = \Pi(h)$. For $\Pi(h)$ of the form (2.2), $U(h)$ is given by

$$U(h) = -\frac{\varepsilon^2}{2h^2} + \frac{\varepsilon^3}{3h^3}. \tag{2.6}$$

A similar energy functional was used in Brusch *et al.* (2002) to study heterogeneous dewetting. Equation (2.5) reduces to the form used in Bertozzi *et al.* (2001) and Glasner (2003) and other papers for the homogeneous problem with $A(x) \equiv 1$. In both cases, E is monotonically decreasing with the same form for the rate of dissipation,

$$\frac{dE}{dt} = -\frac{1}{\bar{A}} \int_0^L h^3 (\partial_x p)^2 \, \mathrm{d}x \leqslant 0, \tag{2.7}$$

showing that the dynamics of (2.3) follow a gradient flow. The mass of the thin film on $[0, L]$ is given by

$$m = \int_0^L h(x,t)\,\mathrm{d}x, \tag{2.8}$$

and is conserved by the dynamics.

We seek solutions $h(x,t)$ that are continuous and whose first derivative is continuous at $x = s$, i.e.

$$\lim_{x\to s^-} h(x,t) = \lim_{x\to s^+} h(x,t) \tag{2.9a}$$

$$\lim_{x\to s^-} \frac{\partial h}{\partial x}(x,t) = \lim_{x\to s^+} \frac{\partial h}{\partial x}(x,t), \tag{2.9b}$$

and locally conserve mass across the wettability jump at $x = s$. These conditions yield that solutions will have a continuous pressure (2.4) but must have a jump in the curvature at $x = s$, i.e.

$$\frac{\partial^2 h}{\partial x^2}(s^+,t) - \frac{\partial^2 h}{\partial x^2}(s^-,t) = (A_2 - A_1)\Pi(h(s,t)). \tag{2.10}$$

Steady-state solutions on homogeneous substrates have been previously analysed in Laugesen & Pugh (2000a,b), Bertozzi *et al.* (2001), Glasner & Witelski (2003), Hutchinson *et al.* (2013), Pahlavan *et al.* (2018) and many other papers. From (2.3) and (2.7), it can be seen that all positive steady-state solutions subject to no-flux boundary conditions have uniform constant pressure, i.e. $p \equiv \bar{p}$. This is still true for heterogeneous substrates where $A(x)$ makes $\tilde{\Pi} = A\Pi$ spatially dependent. It follows that the steady-state solutions of (2.3a) subject to (2.3b) satisfy

$$\frac{d^2 h}{dx^2} = A(x)\Pi(h) - \bar{p}, \tag{2.11a}$$

$$h_x(0) = 0, \qquad h_x(L) = 0. \tag{2.11b}$$

For the homogeneous case, all steady states can be described with respect to the range of the function $\Pi(h)$; spatially uniform solutions ('flat films' $h(x) \equiv \bar{h}$) exist for any positive thickness and correspond to $-\infty < \bar{p} \leqslant p_{\max}$, where $p_{\max} = 27/(256\varepsilon)$ is the maximum of $\Pi(\bar{h})$, attained at $\bar{h} = h_{\text{peak}} = 4\varepsilon/3$. For sufficiently large L, non-trivial steady solutions exist for $0 < \bar{p} < p_{\max}$; see Bertozzi *et al.* (2001). We will see that the situation for heterogeneous substrates is more complicated.

For the heterogeneous case where $A(x)$ is a step function with $A_1 \neq A_2$, for a steady-state solution to be a flat film and satisfy (2.10), the only option is to have $\Pi(\bar{h}) = 0$, yielding $\bar{h} = \varepsilon$. Hence, $h(x) \equiv \varepsilon$ is the only possible flat film solution on a heterogeneous substrate, with corresponding pressure $\bar{p} = 0$.

For the stepwise $A(x)$, the analysis of (2.11) follows from piecewise-defined autonomous phase plane analysis on $0 \leqslant x \leqslant s$ and $s \leqslant x \leqslant L$ with constant $A = A_i$ for $i = 1, 2$, respectively. From the analysis in Bertozzi *et al.* (2001), for the phase plane for (2.11a) with $A \equiv 1$, for $0 < \bar{p} < p_{\max}$ then the problem has two fixed points, a hyperbolic saddle $h = H_{\text{s},i}$ (with $H_{\text{s},i} < h_{\text{peak}}$) and an elliptic centre point $h = H_{\text{c},i}$ (with $H_{\text{c},i} > h_{\text{peak}}$), each satisfying

$$\Pi(H_i) = \frac{\bar{p}}{A_i}. \tag{2.12}$$

There is a homoclinic orbit that passes through the saddle point, defining a single maximal-amplitude droplet on $-\infty < x < \infty$. This solution has $H_{\text{s},i}$ as its global minimum and its corresponding maximum $H_{\max,i}$ is obtained from a first integral, as in Bertozzi *et al.* (2001). In the phase plane, the homoclinic

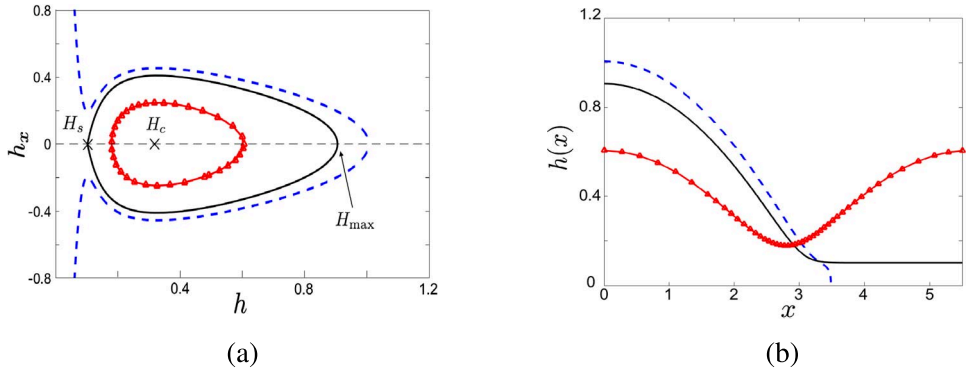

FIG. 2. (a) Phase plane for the homogeneous substrate case, with parameters $\bar{p} = 0.2, \varepsilon = 0.1$, showing trajectories for the homoclinic orbit (solid black curve), a periodic solution (red dotted curve) and a solution that lies outside of the homoclinic orbit (dashed blue curve). (b) Profiles of the three steady-state solutions corresponding to the trajectories shown in (a).

orbit encloses a continuous family of periodic solutions, each having its minimum in the range $H_{s,i} < h_{\min} \leqslant H_{c,i}$ and corresponding maximum in $H_{c,i} \leqslant h_{\max} < H_{\max,i}$.

Figure 2(a) illustrates the trajectories in the phase plane: the homoclinic orbit with $h_x \to 0$ as $h \to H_{s,i}$ (solid black curve), a periodic solution bounded inside the homoclinic orbit (red dotted curve) and a typical solution lying entirely outside of the homoclinic orbit with $|h_x| \to \infty$ and $h \to 0$ at finite x (dashed blue curve) (see also Perazzo *et al.*, 2017). Figure 2(b) shows the profiles corresponding to the three trajectories. On homogeneous substrates, only trajectories that lie inside of the homoclinic orbit yield acceptable steady solutions of (2.3). In this paper, we will show that trajectories that lie outside of the homoclinic orbit will be used to construct steady states of thin films on heterogeneous substrates.

Figure 3(a) shows the numerically computed bifurcation diagram for the film mass vs. the maximum and minimum film thickness, denoted by $h_{\max}$ and $h_{\min}$, for steady solutions on a homogeneous substrate with length $L = 3$. This type of bifurcation diagram has been previously studied in detail by Bertozzi *et al.* (2001). Continuous families of non-trivial (periodic) solutions branch-off from the set of flat films (represented by the diagonal line in Fig. 3(a)) at pairs of pitchfork bifurcation points, $\bar{h} = \bar{h}_{k,\pm}$. The number of loops of solutions, N, depends on the domain size L and the derivative of the disjoining pressure through

$$\Pi'(\bar{h}_k) = -k^2\pi^2/L^2, \qquad k = 1, 2, \cdots, N; \tag{2.13}$$

see Bertozzi *et al.* (2001). For the (ε, L) used here, $N = 2$ yielding two loops corresponding to half- and whole-droplets on $[0, L]$. Figure 3(b) shows the profiles of two droplet solutions with mass $m = 1.1$ centred at opposite ends of the domain. Because of the reflection symmetry under $x \to L - x$ for the homogeneous problem, both of these solutions are given by the same state from the bifurcation diagram.

Figure 3(c) shows the same type of bifurcation diagram as Fig. 3(a), but for thin films on a stepwise-patterned substrate with $A_1 = 1$, $A_2 = 1.1$ and $s = L/2$. The spatial dependence of this disjoining pressure breaks the reflection symmetry and steady-state droplets centred at $x = 0$ and $x = L$ with the same mass now differ in profiles, as illustrated in Fig. 3(d). Compared with the homogeneous case, this symmetry-breaking for the heterogeneous case replaces the pitchfork points with imperfect bifurcations, as seen in Kao *et al.* (2006), and yields more complicated loop structures. The outer loops represent

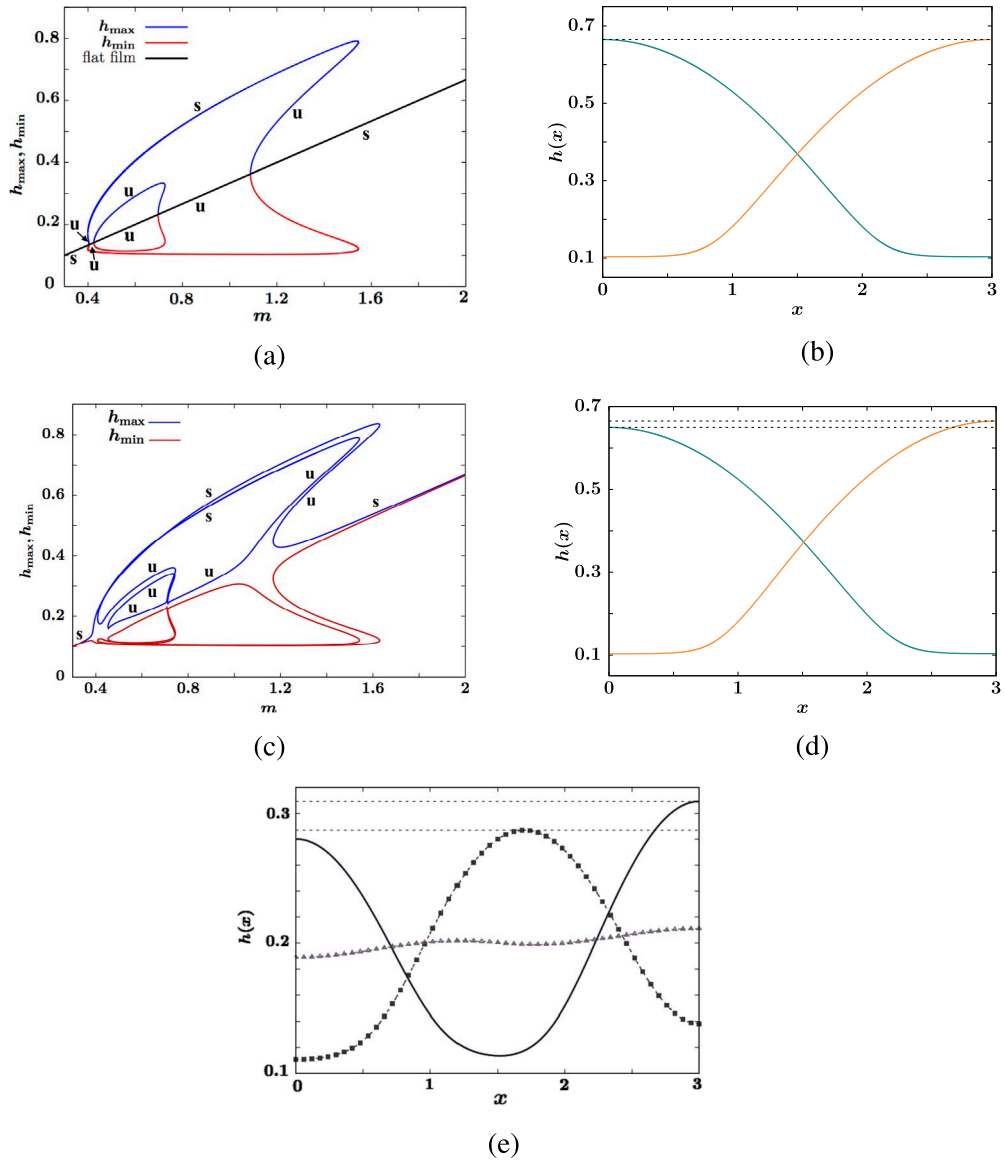

FIG. 3. Steady solutions with $\varepsilon = 0.1$ on a domain of length $L = 3$: (a) Bifurcation diagram for m vs. $h_{\min}$ and $h_{\max}$ for solutions on a homogeneous substrate, $A(x) \equiv 1$. (b) Profiles of two steady-state droplets from (a) with $m = 1.1$ centred at $x = 0$ and $x = L$. (c) Bifurcation diagram for m vs. $h_{\min}, h_{\max}$ for steady-state solutions on a stepwise-patterned substrate with $A_1 = 1, A_2 = 1.1$ and $s = L/2$. (d) The two distinct droplet profiles for the heterogeneous problem, centred at $x = 0$ and $x = L$ both with mass $m = 1.1$. The difference in the maximum film thicknesses is highlighted by the two dashed lines. (e) Profiles of three distinct non-trivial inner loop steady-state solutions on a stepwise-patterned substrate, all with mass $m = 0.6$. In (a) and (c), each branch is labelled 's' or 'u' to indicate the stability. The stability of branches in (c) will be discussed in detail in Section 6.

branches of solutions with maxima at either $x = 0$ or $x = L$, while the inner loops give solutions with interior critical points. Figure 3(e) shows the profile of three distinct steady-state solutions on the inner loop of Fig. 3(c) with the same mass, $m = 0.6$.

For convenience, we focus on solutions that are monotone decreasing, describing a half-droplet profile on $x \in [0, L]$ (which can be symmetrically extended to give a single whole drop on $[-L, L]$, as in Fig. 1). We can write the first integral of (2.11a) on $x \in [0, s]$ and $x \in (s, L]$ as

$$\frac{dh}{dx} = -\begin{cases} \sqrt{2R_1(h)} & 0 \leqslant x \leqslant s, \\ \sqrt{2R_2(h)} & s < x \leqslant L, \end{cases} \tag{2.14a}$$

where

$$\begin{aligned} R_1(h) &= A_1(U(h) - U(h_{\max})) - \bar{p}(h - h_{\max}), \\ R_2(h) &= A_2(U(h) - U(h_{\min})) - \bar{p}(h - h_{\min}). \end{aligned} \tag{2.14b}$$

Equation (2.14a) along with the condition (2.9b) yields a condition relating the film thickness at the heterogeneity interface, $x = s$, to the extrema for steady states on stepwise-patterned substrates with $A(x)$ of the form (2.1),

$$(A_1 - A_2)U(h(s)) + \bar{p}(h_{\max} - h_{\min}) = A_1 U(h_{\max}) - A_2 U(h_{\min}), \tag{2.15}$$

which we will use for later analysis. Setting both As to A_i and using $h_{\min} = H_{s,i}$ reduce (2.15) to the first integral equation for $h_{\max} = H_{\max,i}$.

3. Classification of branches in the bifurcation diagram in one dimension

For the remainder of the article, we use a different form of the bifurcation diagram that facilitates describing the effects due to heterogeneous wettability. Figure 4 shows numerically computed bifurcation diagrams of $\bar{p}$ vs. $h_{\max}$ for steady states on homogeneous and heterogeneous substrates on a domain of length $L = 3$ with $\varepsilon = 0.1$. Here, in the homogeneous case, all flat films are represented by the graph of the disjoining pressure, $\bar{p} = \Pi(h_{\max})$ (dotted curve). The branch of non-trivial solutions bifurcating from the flat films in Fig. 4(a) corresponds to the outer loop from Fig. 3(a). The inset plot shows that the branch bifurcates slightly below $p_{\max}$.

For the heterogeneous case, we consider a typical problem with $A_2 = 5$, $s = L/2 = 1.5$ and similarly plot solutions corresponding to the analogous outer loop from Fig. 3(c). We observe that the family of solutions is continuous and smooth and has fold points separating the curve into six segments; see Fig. 4(b). We will analyse the dependence of solutions in each of these segments with respect to limits for ε and A_2. In Section 3, we will use bifurcation diagrams for $\bar{p}$ vs. $h_{\max}$, instead of the diagram m vs. $h_{\min}, h_{\max}$ shown in Section 2, to classify and describe the different types of steady-state solutions for two reasons. First, each family of steady-state solutions corresponds to one segment of the bifurcation curve $\bar{p}$ vs. $h_{\max}$ in the limit of small ε, as mentioned above. Second, this form of diagram shows the explicit dependence on the pressure $\bar{p}$ and will be more direct for illustrating the asymptotic results derived for each type of steady state parametrized by $\bar{p}$.

Although there is no more flat film solution except for $h(x) \equiv \varepsilon$ with $\bar{p} = 0$ for $A_1 \neq A_2$, as we will show later in Section 3.1, branches 1 and 6 yield nearly flat films that are perturbations of the flat

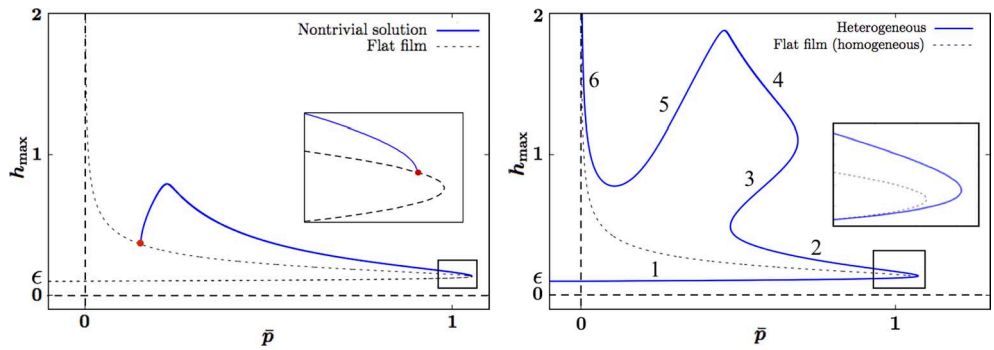

FIG. 4. Bifurcation diagram for $\bar{p}$ vs. $h_{\max}$ for steady states with $\varepsilon = 0.1$ and $L = 3$ on (a) a homogeneous substrate, $A(x) \equiv 1$, (b) on a heterogeneous substrate with $A_1 = 1, A_2 = 5, s = 1.5$. The solid blue curve represents nontrivial steady-state solutions. The dashed black curve in (a) represents two branches of flat film solutions that merge together with the nontrivial branch at $\bar{p} = p_{\max}$. In both (a) and (b), the inset plot shows the bifurcation curve zoomed into a small neighbourhood of the maximum pressure. The red dots in the inset plot of (a) denote the bifurcation points.

film solutions. Figure 4(b) includes the graph of $\Pi(h_{\max})$ for reference, to show that the heterogeneous bifurcation diagram approaches that curve for the limits of large and small film thickness. From the inset, it is notable that the branch extends to a value of $\bar{p}$ slightly greater than $p_{\max}$.

In the following subsections, we will present our analysis and computations of these steady-state solutions by branch. For each branch, we develop an asymptotic prediction for the steady-state profile and show that the leading-order solution for each branch depends on different parameters in (L, s, A_1, A_2), which describe the chemical heterogeneity of the substrates.

Based on the structure of the diagram shown in Fig. 4(b), we divide the steady-state solutions that could exist on a heterogeneous substrate with patterning $A(x)$ of the form (2.1) into six different connected branches, as follows.

- Branch 1: small-thickness films
- Branch 2: small-width droplets
- Branch 3: pinned droplets
- Branch 4: large-width droplets
- Branch 5: confined droplets
- Branch 6: large-thickness films

Branches 1 and 6 are perturbations of homogeneous flat films while branches 2, 4 and 5 correspond to non-trivial droplet solutions. And in particular, branch 3 is an entirely new branch of solutions characterizing a class of 'pinned' drops that emerges due to the presence of chemical heterogeneity.

3.1 *Small-thickness and large-thickness nearly flat films*

In this subsection, we study two types of solutions that are perturbations of flat films. First, we study branch 1, which gives steady-state solutions with mean thickness $h = O(\varepsilon)$. Two examples of steady-

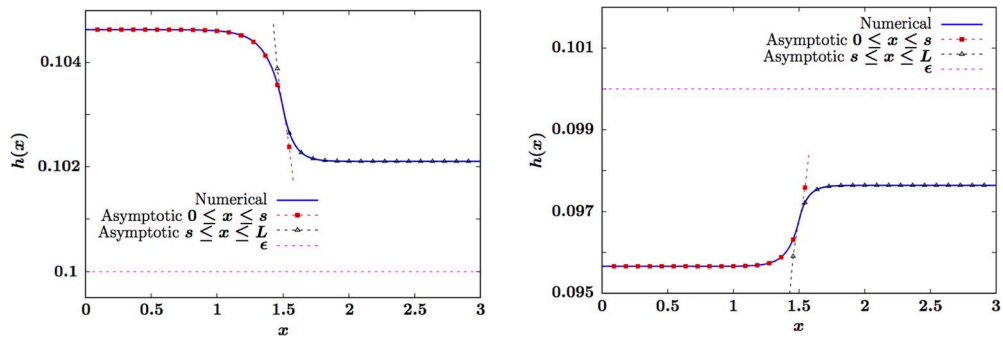

FIG. 5. Branch 1, small-thickness film solutions, computed with parameters $A_1 = 1, A_2 = 2, s = 1.5, \varepsilon = 0.1$. (a) A numerical solution (blue) with $\bar{p} = 0.387$ having mean thickness $\bar{h} > \varepsilon$ compared with approximate form (3.3) (dotted curves). (b) A computed solution (blue) with $\bar{p} = -0.518$ yielding mean thickness $\bar{h} < \varepsilon$ also compared with (3.3).

state profiles of this type of small-thickness films are given in Fig. 5. Both solutions are characterized by nearly flat films away from the patterning interface $x = s$ and a rapid change in the profile in a small neighbourhood of the interface $x = s$. The rapid change in $h(x)$ near the interface is due to the large change in disjoining pressure for films of thickness $h = O(\varepsilon)$. The disjoining pressure $\Pi(h)$ increases rapidly for h in the range $0 < h < 4\varepsilon/3$ in the limit $\varepsilon \to 0$. The mean film thickness of branch 1 solutions falls within this range.

These solutions can be understood using matched asymptotics for $\varepsilon \to 0$. Away from $x = s$, the second derivative in (2.11a) can be neglected and the outer solutions to all orders are given by the respective saddle points,

$$h_{\text{out}}(x) = \begin{cases} H_{\text{s},1} & 0 \leqslant x \leqslant s, \\ H_{\text{s},2} & s < x \leqslant L, \end{cases} \tag{3.1}$$

where

$$H_{\text{s},i} = \varepsilon + \frac{\varepsilon^2 \bar{p}}{A_i} + O(\varepsilon^3) \tag{3.2}$$

with $\bar{p} = O(1)$. In an $O(\varepsilon)$ neighbourhood of $x = s^{\pm}$, the solution satisfies a non-linear boundary layer equation (balancing the disjoining pressure and the second derivative). However, rather than pursuing this approach to the analysis, we can take advantage of the fact that the range of the solution is small, $h_{\max} - h_{\min} = O(\varepsilon^2)$, to estimate the local behaviour from a linearized analysis.

Linearizing (2.11a) about each saddle yields the approximate form of the solution as

$$h(x) \approx \begin{cases} H_{\text{s},1} + C_1 e^{\sqrt{A_1 \Pi'(H_{\text{s},1})}\,(x-s)} & 0 \leqslant x \leqslant s, \\ H_{\text{s},2} + C_2 e^{-\sqrt{A_2 \Pi'(H_{\text{s},2})}\,(x-s)} & s < x \leqslant L, \end{cases} \tag{3.3}$$

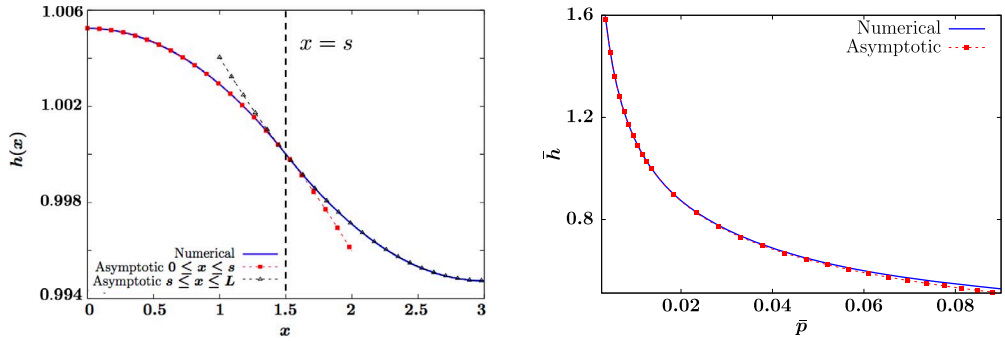

FIG. 6. Branch 6, thick film solutions, computed for parameters $\varepsilon = 0.1$, $A_1 = 1$, $A_2 = 2$, $L = 3$, $s = 1.5$. (a) A numerically computed solution (blue) compared with the asymptotic estimates (3.5) (dotted) at pressure $\bar{p} = 0.0135$. (b) The computed mean thickness $\bar{h}$ (blue) as a function of $\bar{p}$ compared with the asymptotic prediction (3.7) (red dots).

with constants C_1, C_2 to be determined from conditions (2.9a) and (2.9b). Solving for C_i shows that for $A_1, A_2 = O(1)$, $C_i = O(\varepsilon^2\bar{p})$ so $C_i \ll H_{s,i}$ as long as $\bar{p} \ll \varepsilon^{-1}$. For $A_1 = O(1)$ and $A_2 \to \infty$, similarly $C_1 = O(\varepsilon^2\bar{p}) \ll H_{s,1}$ and $C_2 = O\left(\varepsilon^2\bar{p}/\sqrt{A_2}\right) \ll H_{s,2}$ for $\bar{p} \ll \varepsilon^{-1}$.

We note that for $\bar{p} > 0$, the saddle points are related by $H_{s,1} > H_{s,2}$ yielding monotone decreasing profiles; this inequality is reversed for $\bar{p} < 0$ (hence, the monotone increasing solution in Fig. 5(b)) with the flat-film solution $h \equiv \varepsilon$ being the transition state at $\bar{p} = 0$.

Figure 5(a) shows a small-thickness solution with mean thickness $\bar{h} > \varepsilon$ (corresponding to $\bar{p} > 0$), where we define $\bar{h} = \int_0^L h\,\mathrm{d}x/L$ (specifically $\bar{p} = 0.387$ corresponds to $m = 0.31$ and $m/L > \varepsilon$ for $L = 3$). Figure 5(b) shows the profile for another branch 1 solution, with $\bar{p} < 0$ yielding $\bar{h} < \varepsilon$. In Fig. 5(a and b), the boundary layer near $x = s$ can be well approximated by the estimate (3.3).

For $\bar{p} < 0$, equation (2.12) has only one root with $H_{s,i} < \varepsilon$ and for $\bar{p} \to -\infty$ its leading order behaviour is $H_{s,i} \sim \varepsilon^{3/4}(A_i/|\bar{p}|)^{1/4}$. Consequently the solutions on branch 1 in this limit can still be approximated by the smoothed step profile (3.3), but now the range of the solutions is $h_{\max} - h_{\min} = O(|\varepsilon^3/\bar{p}|^{1/4})$ and the width of the interior transition layer is $O(|\bar{p}|^{-5/8})$.

The limit $\bar{p} \to 0^+$ also describes another class of solutions, characterized by nearly-flat films with large thickness, corresponding to branch 6 in Figure 4(b). Unlike thin nearly-flat solutions, which have a boundary layer near $x = s$ and approach a step function in the limit $\varepsilon \to 0$, this class of thick solutions has small amplitude slowly-varying deviations from the mean film thickness. An example of a steady-state profile on this branch is shown in Figure 6(a).

We write $\bar{h} = m/L$ in terms of the mass of the solution, $m = \int_0^L h\,dx$. For $\bar{h} \to \infty$, we write the solution as $h(x) \sim \bar{h} + \sigma h_1(x) + \sigma^2 h_2(x)$ and we will show that it is convenient to define $\sigma = \Pi(\bar{h})$. From (2.2), it is clear that the limit $\bar{h} \to \infty$ for any fixed ε is equivalent to $\sigma \to 0$.

Substituting this expansion into equation (2.11a) and expanding $\Pi(h)$ to $O(\delta)$, we have

$$\sigma h_{1xx} = \sigma A_1 + \sigma A_1 \Pi'(\bar{h}) h_1 - \bar{p}, \qquad h_{1x}(0) = 0, \qquad 0 < x \leqslant s, \tag{3.4a}$$

$$\sigma h_{1xx} = \sigma A_2 + \sigma A_2 \Pi'(\bar{h}) h_1 - \bar{p}, \qquad h_{1x}(L) = 0, \qquad s < x \leqslant L. \tag{3.4b}$$

To balance the equation at $O(\sigma)$, we choose $\bar{p} = O(\sigma)$ by writing $\bar{p} \sim \sigma(p_0 + \sigma p_1)$ for some $p_0 = O(1)$. As $m \to \infty$, $\Pi'(\bar{h}) < 0$. Solving for $h_1(x)$ on $0 \leqslant x \leqslant s$ and $s < x \leqslant L$, respectively, we obtain to $O(\sigma)$

$$h(x) \sim \begin{cases} \bar{h} + \Pi(\bar{h}) \left(C_1 \cos(r_1 x) + \frac{A_1 - p_0}{r_1^2} \right) & 0 \leqslant x \leqslant s, \\ \bar{h} + \Pi(\bar{h}) \left(C_2 \cos(r_2 (L - x)) + \frac{A_2 - p_0}{r_2^2} \right) & s < x \leqslant L, \end{cases} \tag{3.5}$$

where $r_i = \sqrt{-A_i \Pi'(\bar{h})}$. To determine constants C_1 and C_2, we use conditions (2.9a) and (2.9b). Consequently, we find that C_1 and C_2 are both linear in p_0, $C_1 = p_0 \tilde{C}_1$ and $C_2 = p_0 \tilde{C}_2$. The definition of the mean thickness $\bar{h}$ yields the condition $\int_0^L h_1(x)\, \mathrm{d}x = 0$, which we can solve for p_0 to obtain

$$\bar{p} \sim \frac{\Pi(\bar{h}) L}{\frac{s}{A_1} + \frac{L - s}{A_2} + \frac{\tilde{C}_1 \Pi'(\bar{h})}{r_1} \sin(r_1 s) + \frac{\tilde{C}_2 \Pi'(\bar{h})}{r_2} \sin(r_2 (L - s))}. \tag{3.6}$$

Simplifying (3.6) further, in the limit of large $\bar{h}$, the pressure can be written as

$$\bar{p} = \left(A_1 \frac{s}{L} + A_2 \frac{L - s}{L} \right) \left(\frac{\varepsilon^2}{\bar{h}^3} - \frac{\varepsilon^3}{\bar{h}^4} \right) + O(\bar{h}^{-7}). \tag{3.7}$$

This result being in terms of the weighted average of the wetting parameters A_i with respect to domain lengths can be interpreted as giving an effective overall leading-order disjoining pressure $\tilde{\Pi}$ for the nearly flat film homogenized at the mean level $\bar{h}$: $\tilde{\Pi} \sim \bar{A} \Pi(\bar{h})$. The higher-order terms in (3.7) contain factors of $(A_1 - A_2)$ and $s(L - s)$ so if the problem was on a homogeneous substrate (via $A_2 = A_1$ or $s = 0$ or $s = L$), then this trivially reduces to the disjoining pressure for a flat film.

Figure 6(a) shows a typical branch 6 thick film solution computed at pressure $\bar{p} = 0.0135$. The asymptotic estimate given by (3.5) agrees very well with the numerical solution, which suggests that $\bar{p}$ is inversely proportional to m^3 for large mass. For fixed large mass, $\bar{p}$ scales linearly in both A_1 and A_2. Figure 6(b) shows $\bar{h}$ for numerically computed branch 6 solutions over a range of $\bar{p}$. The comparison with the analytical predictions show that (3.7) is accurate for the limit of large $\bar{h}$.

3.2 *Large-width and confined droplets*

In this subsection, we study branches 4 and 5, which give two families of droplet-type solutions that are similar to droplet solutions on homogeneous substrates. Droplets are states where most of the fluid is concentrated within a region of limited width (or radius) and is surrounded by nearly uniform very thin films with thickness $h = O(\varepsilon)$ set by the disjoining pressure.

First, we discuss branch 4, which describes a class of large-width droplets with width $s < w < L$. On the droplet core, we assume $h = O(1)$ on $0 \leqslant x < w$, and $h = O(\varepsilon)$ outside. One example of such a steady-state solution is shown by the blue curve in Fig. 7. We show that in the limit $\varepsilon \to 0$, the profiles for these droplets can be approximated to leading order by truncations of the homoclinic droplet on the homogeneous substrate with $A(x) \equiv A_2$.

To obtain an asymptotic estimate of the droplet's maximum ($h_{\max} = O(1)$), we use (2.15) in the limit $\varepsilon \to 0$. Since the wetting interface, $x = s$, occurs within the droplet's core, we have $h(s) = O(1)$.

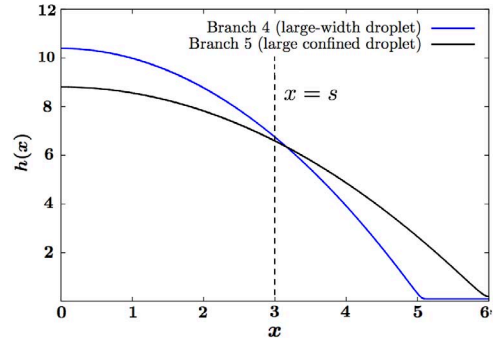

FIG. 7. Profiles of two droplet solutions with mass $m = 35.2$ on the domain $L = 6$ for a disjoining pressure with $A_1 = 1, A_2 = 50$, $L = 6$, $s = 3$, $\varepsilon = 0.1$. A branch 4 large-width droplet, with $s < w < L$, is shown by the blue curve for $\bar{p} = 0.493$ and a branch 5 confined droplet, with $w = L$, at pressure $\bar{p} = 0.809$ is given by the black curve.

For $h = O(1)$, equation (2.6) gives $U(h) = O(\varepsilon^2)$. Using this for $h_{\max}$ and $h(s)$ with $h_{\min} \sim \varepsilon$, equation (2.15) reduces to

$$\bar{p}h_{\max} = -A_2 U(h_{\min}) + O(\varepsilon), \tag{3.8}$$

which gives the inverse dependence on the pressure,

$$h_{\max} = \frac{A_2}{6\bar{p}} + O(\varepsilon). \tag{3.9}$$

Note that to leading order this matches $H_{\max,2}$, the maximum of the homoclinic droplet on a homogeneous substrate with $A(x) \equiv A_2$, as shown in Glasner & Witelski (2003). Since $A_2 > A_1$, this $h_{\max}$ describes a droplet larger than the homoclinic for a homogeneous substrate with $A = A_1$.

For $h = O(1)$, the disjoining pressure scales as $\Pi(h) = O(\varepsilon^2)$, so to leading order (2.11) on the droplet core reduces to $\frac{d^2h}{dx^2} = -\bar{p}$, yielding the parabolic profile

$$h(x) = h_{\max} - \frac{1}{2}\bar{p}x^2 + O(\varepsilon). \tag{3.10}$$

The width can then be estimated from $h(w) = O(\varepsilon)$ as

$$w \sim \sqrt{\frac{A_2}{3\bar{p}^2}}, \tag{3.11}$$

similar to results in Glasner & Witelski (2003). In summary, in the limit $\varepsilon \to 0$, the leading-order profile of a large-width droplet on $[0, L]$ is given by

$$h(x) \sim \begin{cases} \frac{A_2}{6\bar{p}} - \frac{1}{2}\bar{p}x^2 & 0 \leqslant x < w, \\ \varepsilon & w < x \leqslant L. \end{cases} \tag{3.12}$$

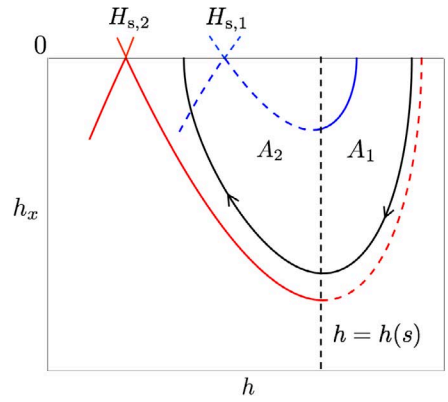

FIG. 8. Schematic of the lower half of the phase plane showing the monotone decreasing portions of the homoclinic orbits for homogeneous substrates, $A(x) \equiv A_1$ (blue) and $A(x) \equiv A_2$ (red) and a branch 4 heterogeneous solution (black), for parameter values $A_1 = 1, A_2 = 2, L = 6, s = 3, p = 0.211, \varepsilon = 0.1$. The value of $A(x)$ switches across the line $h = h(s)$, the 'inactive' portions of the homoclinics are drawn with dashed lines.

The even extension of this profile gives a $2L$-periodic solution and hence its minimum must satisfy $h_{\min} > H_{s,2}$.

In the phase plane, branch 4 solutions lie inside the A_2-homogeneous homoclinic orbit; see Fig. 8. This result is based on two observations for the segments on $x \leqslant s$ and $x > s$. For $x \geqslant s$ (where $h(x) \leqslant h(s)$), this follows directly from the solution's minimum being above the saddle point, $h_{\min} > H_{s,2}$. For $x \leqslant s$ (where $h(x) \geqslant h(s)$), the trajectory lies outside the A_1-homogeneous homoclinic orbit since it starts from $h_{\max} > H_{\max,1}$. To see that this portion lies within the region in the phase plane bounded by the A_2-homoclinic, we use (2.14a) noting that $R_2(h(s)) = R_1(h(s))$ by (2.9b) and $R_2(h) > R_1(h)$ for $h > h(s)$ when $A_2 > A_1$, hence $h_{\max} < H_{\max,2}$.

Branch 4 droplet solutions are defined by their widths exceeding the wetting interface position, $w > s$, but not filling the whole domain, $w < L$. Using (3.11), this yields the range of pressures for branch 4 as $\sqrt{A_2/(3L^2)} \leqslant \bar{p} \leqslant \sqrt{A_2/(3s^2)}$. At the endpoints, this branch connects to other branches of solutions: at $\bar{p}^*_{3,4} = \sqrt{A_2/(3s^2)}$ with droplets pinned at the wetting interface (called branch 3, to be described in the next section) and at $\bar{p}^*_{4,5} = \sqrt{A_2/(3L^2)}$ with droplets limited by the size of the domain (called branch 5, described below). Figure 9 gives the bifurcation diagram for $\bar{p}$ vs. $h_{\max}$, showing good agreement of the numerically computed results and compared with the asymptotic predictions. In the derivation, we assumed $A_1, A_2 = O(1)$; it can be shown that the profile of branch 4 solutions is still described by (3.12) for $A_1 = 1$ fixed and $A_2 \to \infty$, as suggested by Fig. 9(b).

These solutions have mass and width both decreasing with increasing pressure. For $\varepsilon \to 0$, the mass of the droplet core is

$$m \sim \int_0^w h \, \mathrm{d}x \sim \frac{A_2^{3/2}}{9\sqrt{3}\,\bar{p}^2}. \tag{3.13}$$

Note the film mass $m^*_{4,5} \sim \sqrt{3A_2}\,L^2/9$ corresponding to $p^*_{4,5}$ is the maximum possible mass for a droplet-type solution with domain-size L. Above that mass, only nearly flat film solutions (branch 6) exist. The scaling of this critical mass with A_2 shows the importance of the heterogeneous disjoining pressure in controlling droplet structure.

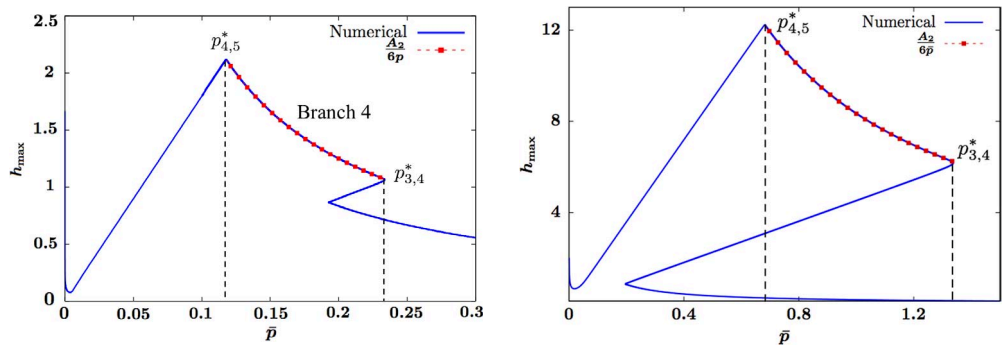

FIG. 9. Bifurcation diagram for $\bar{p}$ vs. $h_{\max}$ computed numerically and compared with the asymptotic prediction of branch 4 (a) in the limit $\varepsilon \to 0$, with parameters $A_1 = 1, A_2 = 1.5, \varepsilon = 0.001$. (b) In the limit $A_2 \to \infty$, with parameters $A_1 = 1, A_2 = 50$, $\varepsilon = 0.01$. In both (a) and (b), $L = 6$, $s = 3$. The blue solid curve represents the numerically computed bifurcation curve. The red dashed and dotted curve represents the asymptotic prediction given by (3.9).

Another important physical property characterizing fluid droplets is the contact angle or angle of inclination at the edge of support. The small aspect ratio assumption essential to lubrication theory justifies use of the small angle approximation, $\tan\theta \sim \theta$, for this context. Consequently, the contact angle scales the slope of the droplet profile at the edge of the core, with the constant of proportionality being the aspect ratio. We see that the effective contact angle of all branch 4 droplets is independent of the pressure,

$$\theta \propto |h'(w)| \sim \bar{p}w = \sqrt{\frac{A_2}{3}}, \tag{3.14}$$

again indicating the controlling influence of the disjoining pressure, as in Glasner & Witelski (2003). It was previously shown in Glasner & Witelski (2003) that large droplets on a homogeneous substrate with $A \equiv 1$ have contact angle given by $|h'(w)| \sim 1/\sqrt{3}$, in agreement with (3.14) when $A_1 = A_2 = 1$.

Branch 5 describes large droplets confined by the domain size so the droplet width is always $w = L$. This set of solutions provides a transition between the large-thickness nearly flat films (branch 6) and the large-width droplets (branch 4) described above. An example of a solution on branch 5 is shown by the black curve in Fig. 7.

We first investigate the solutions in the limit $\varepsilon \to 0$ for $A_1, A_2 = O(1)$. As with branch 4, on the core region ($0 \leqslant x < L$), branch 5 droplets have $h = O(1)$ and the influence of the disjoining pressure can be neglected to yield a parabolic profile, $h(x) = h_{\max} - \frac{1}{2}\bar{p}x^2 + O(\varepsilon)$. Here, using $w = L$ gives the drop's maximum as scaling linearly with the pressure,

$$h_{\max} = \frac{1}{2}\bar{p}L^2 + O(\varepsilon). \tag{3.15}$$

To obtain an asymptotic estimate of the minimum film thickness $h_{\min}$, we use (2.15) and assume $h_{\min} = O(\varepsilon)$. At leading order, the equation reduces to

$$-A_2 U(h_{\min}) = \bar{p}h_{\max} \sim \frac{1}{2}\bar{p}^2 L^2, \tag{3.16}$$

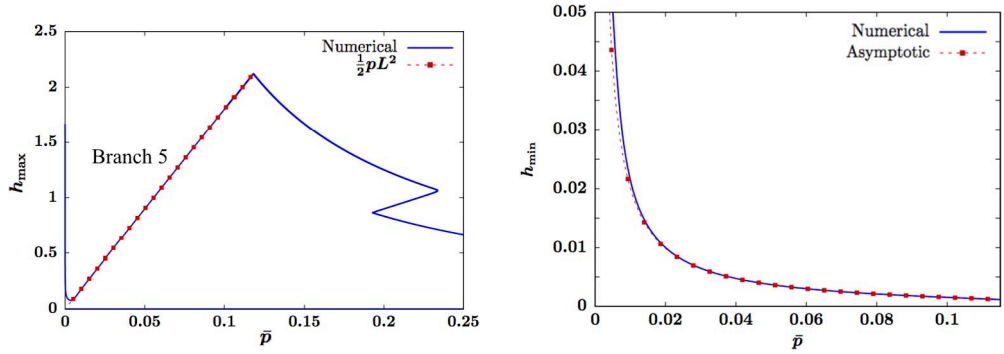

(a) (b)

FIG. 10. Properties of branch 5 large drop solutions computed with parameter values $A_1,\ A_2 = 1.5,\ L = 6,\ s = 3,\ \varepsilon = 0.001$. (a) Branch 5 highlighted in the bifurcation diagram for $\bar{p}$ vs. $h_{\max}$ computed numerically (blue solid curve) and compared with the asymptotic estimate (3.15) (red dotted curve) in the limit of small ε. (b) The minimum, $h_{\min}$ as a function of $\bar{p}$ computed numerically (blue solid curve) and the asymptotic result ((3.17), (3.18)) (red dotted curve).

similarly to (3.8). Note that the potential function $U(h)$ has a global minimum at $h = \varepsilon$ with $U(\varepsilon) = -1/6$. For (3.16) to have a real solution, we need $\frac{1}{2A_2}\bar{p}^2L^2 \leqslant \frac{1}{6}$. This upper bound on the pressure on branch 5 coincides with the lower bound for the pressure on branch 4 found above, $\bar{p}^*_{4,5} = \sqrt{A_2/(3L^2)}$. With $U(h)$ of the form (2.6), (3.16) can be written as a cubic polynomial equation,

$$\frac{1}{2}y^2 - \frac{1}{3}y^3 = z \qquad \text{with} \qquad y = \frac{\varepsilon}{h_{\min}}, \qquad z = \frac{\bar{p}^2L^2}{2A_2}. \tag{3.17}$$

The solution for $h_{\min}$ on $0 \leqslant z \leqslant 1/6$ is the smaller of the two positive roots for y, given by

$$y = \frac{1}{2}\left(1 - \frac{1+i\sqrt{3}}{2}\sigma - \frac{1-i\sqrt{3}}{2\sigma}\right) \qquad \text{with} \qquad \sigma = \left(1 - 12z + 12\sqrt{z^2 - z/6}\right)^{1/3}, \tag{3.18}$$

where σ is complex-valued yielding $y \sim 1$ for $z \to 1/6$ and $y \sim \sqrt{2z}$ as $z \to 0$.

For $y = O(1)$, it is clear that $h_{\min} = \varepsilon/y = O(\varepsilon)$, consistent with our earlier assumption. This result holds for solutions on branch 5 with the pressure bounded away from zero, with $\bar{p} < \bar{p}^*_{4,5}$. Branch 6 is approached as $\bar{p} \to 0$. Figure 10(a and b) shows the plots for $\bar{p}$ vs. $h_{\max}$ and $\bar{p}$ vs. $h_{\min}$ computed numerically and asymptotically in the limit of small ε for $A_1, A_2 = O(1)$.

A uniform solution for the droplet can be constructed using matched asymptotics (Kevorkian & Cole, 1996) in the limit of $\varepsilon \to 0$ with the parabolic profile, (3.10) with (3.15), being the outer solution on $0 \leqslant x < L$. To leading order, this outer solution gives the mass and effective contact angle of the droplet as

$$m \sim \frac{1}{3}\bar{p}L^3, \qquad \theta \propto |h'(L)| \sim \bar{p}L. \tag{3.19}$$

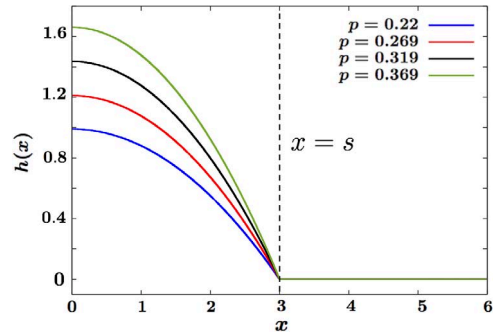

FIG. 11. Typical pinned droplet branch 3 solutions for $A_1 = 1, A_2 = 50, s = 3, L = 6$ at several values of $\bar{p}$.

Note that for $\bar{p} \to 0$, the vanishing contact angle is consistent with the branch of droplets transitioning to become the branch of thick films (branch 6) with $h_{\min} \gg O(\varepsilon)$.

To satisfy the boundary condition $h'(L) = 0$ at the edge of the domain, the solution must have a corner layer to give a rapid transition from the finite contact angle (3.19). The local structure for $\varepsilon \to 0$ will actually be a triple deck (Murdock, 1999) with an inner solution of the form $h = \varepsilon H(X)$ with $X = (x - L)/\varepsilon$ satisfying

$$\frac{d^2H}{dX^2} = \frac{A_2}{H^3}\left(1 - \frac{1}{H}\right) - \varepsilon\bar{p}, \tag{3.20}$$

nested within an intermediate layer $h = \varepsilon^{2/3}\hat{H}(\hat{X})$ with $\hat{X} = (x - L)/\varepsilon^{1/3}$ satisfying

$$\frac{d^2\hat{H}}{d\hat{X}^2} = \frac{A_2}{\hat{H}^3}\left(1 - \frac{\varepsilon^{1/3}}{\hat{H}}\right) - \bar{p}. \tag{3.21}$$

From (3.21), the inflection point will occur in the intermediate layer, with $h \sim (\varepsilon^2 A_2/\bar{p})^{1/3}$; this could be used to obtain a refined estimate of the contact angle. We will not go into the details of this construction here. Note that when $h_{\min} = O(\varepsilon^{2/3})$ the triple deck should reduce to just the intermediate layer and give an estimate for the lower bound on $\bar{p}$ where the above arguments apply.

3.3 *Pinned droplets*

Solutions on branch 3 are droplets with width pinned by the wetting heterogeneity, $w \sim s$, and $h = O(\varepsilon)$ for $x \geqslant s$. Examples of branch 3 profiles for several values of the pressure are shown in Fig. 11. This branch arises as a consequence of the chemical heterogeneity of the substrate. These solutions have several features in common with the confined droplets from branch 5, differences stem from whether the width is pinned by boundary conditions or the wetting contrast. To develop an asymptotic prediction for this type of solutions, we consider the steady state in the limits $\varepsilon \to 0$ and $A_2 \to \infty$.

We consider the solution in the limit $\varepsilon \to 0$ with fixed $A_1, A_2 = O(1)$. On $0 \leqslant x \leqslant s$, the solution will satisfy the equation

$$\frac{d^2h}{dx^2} = \frac{\varepsilon^2 A_1}{h^3}\left(1 - \frac{\varepsilon}{h}\right) - \bar{p}. \tag{3.22}$$

Similar to branch 5 solutions, the disjoining pressure can be neglected at $O(1)$ and $O(\varepsilon)$ to yield a parabolic profile for the droplet core, (3.10). Since the droplet has width $w \sim s$, to leading order, the maximum is given by $h_{\max} \sim \frac{1}{2}\bar{p}s^2$ and to $O(\varepsilon)$ the solution can be written as

$$h(x) \sim \frac{1}{2}\bar{p}\left(s^2 - x^2\right) + \varepsilon C_0 \qquad \text{on } 0 \leqslant x < s. \tag{3.23}$$

Since the leading-order term in this outer solution vanishes as $x \to s^-$, a boundary layer is needed to prevent the divergence of the disjoining pressure contribution there. The structure of inner solution at $x = s^-$ follows similarly to the corner layer at $x = L$ for confined drops in the previous section except here the coefficient on the disjoining pressure term will be A_1 and $\bar{p}$ will be shown to be $O(1)$ on the whole branch of solutions.

Using (2.15) with $h_{\max} = O(1)$ and $h_{\min} \sim \varepsilon$, at leading order, we get a cubic equation for the thickness at the wetting interface,

$$U(h(s)) = \frac{-\frac{A_2}{6} + \frac{1}{2}\bar{p}^2 s^2}{A_2 - A_1} \tag{3.24}$$

with $h(s)$ being the real positive root with $h(s) > \varepsilon$. Similarly to (3.17), such a solution will exist only if $-1/6 < U(h(s)) < 0$, yielding a condition on the range of pressures for branch 3,

$$\sqrt{\frac{A_1}{3s^2}} < \bar{p} < \sqrt{\frac{A_2}{3s^2}}\,, \tag{3.25}$$

where the upper bound matches $\bar{p}^*_{3,4}$ for branch 4 solutions, found in Section 3.2. While the maximum height for these drops scales linearly with the pressure $\bar{p}$, we will see that the contact angle is a bit more complicated to interpret.

To obtain information about the structure of the solution at the contact line, we re-examine the solution in the limit of $A_2 \to \infty$. Let $\delta = 1/A_2$, then we can write equation (2.11a) on $s \leqslant x \leqslant L$ as

$$\delta\frac{d^2h}{dx^2} = \Pi(h) - \delta\bar{p}. \tag{3.26}$$

For $\delta \to 0$ this is a singularly perturbed problem that can be solved using the method of matched asymptotic expansions in terms of an outer solution and a boundary layer of width $O(\delta^{1/2})$. The boundary conditions, (2.9) and $(2.11b)_2$, determine that the boundary layer must be at $x = s^+$. The outer solution of (3.26) for $s < x \leqslant L$ is a constant to all orders,

$$h(x) = \varepsilon + \delta\varepsilon^2\bar{p} + O(\delta^2); \tag{3.27}$$

this is the $\delta \to 0$ expansion of the saddle point $H_{s,2}$, (3.2). Hence, apart from exponentially small terms, the solution's minimum is $h_{\min} \sim H_{s,2}$.

The form of the inner solution in the boundary layer is $h = \hat{h}(\hat{x})$ where $\hat{x} = (x - s)/\delta^{1/2}$ and (3.26) becomes

$$\frac{d^2\hat{h}}{d\hat{x}^2} = \Pi(\hat{h}) - \delta\bar{p}. \tag{3.28}$$

The inner solution must match (3.27) for $\hat{x} \to \infty$ and satisfy (2.9) at $\hat{x} = 0$. Noting that for $A_2 \to \infty$, $h_{\max} = O(1)$ and $h_x(s^-) = O(1)$ from $(2.14a)_1$, there may be concern that the form of $R_2(h)$ suggests that $h_x(s^+) = O(\delta^{-1/2})$. However, from (2.9b), it must be the case that $h_x(s^+) = h_x(s^-) = O(1)$; applied to R_2, this forces $U(h) - U(h_{\min}) = O(\delta)$. Consequently, the expansion of the inner solution must be $\hat{h}(\hat{x}) = \varepsilon + \delta^{1/2}\hat{h}_1(\hat{x}) + O(\delta)$ where $\hat{h}_1$ satisfies the linearized equation, $\hat{h}_{1\hat{x}\hat{x}} = \Pi'(\varepsilon)\hat{h}_1$. To satisfy matching, this term must be an exponential decay, $\hat{h}_1(\hat{x}) = C_2 e^{-\hat{x}/\varepsilon}$, and overall

$$h(x) \sim \varepsilon + \delta^{1/2} C_2 e^{-(x-s)/(\varepsilon\delta^{1/2})} \qquad s \leqslant x < L. \tag{3.29}$$

To determine the C_2 coefficient, we re-write (3.24) as

$$U(h(s)) = \frac{-\frac{1}{6} + \frac{1}{2}\delta\bar{p}^2 s^2}{1 - \delta A_1} \tag{3.30}$$

and plug in $h(s) \sim \varepsilon + \delta^{1/2} C_2$. Expanding for $\delta \to 0$, we get

$$h(s) \sim \varepsilon + \frac{\varepsilon}{\sqrt{A_2}}\sqrt{\bar{p}^2 s^2 - \frac{A_1}{3}}. \tag{3.31}$$

This result can also be obtained as the leading-order approximation from solving (3.30) as a cubic equation as was done with (3.17). Figure 12(a) shows numerically computed values and the asymptotics for $h(s) - \varepsilon$ compared with the asymptotic approximation given by (3.31) for large A_2.

Using the asymptotic prediction (3.31), we can also derive $h'(s)$, which represents the contact angle of this class of droplets in the limit of large A_2. On the A_1 region $[0, s]$, as $x \to s^-$, using (2.14a), we have

$$\frac{1}{2}h'(s)^2 = A_1 U(h(s)) - \bar{p}h(s) + \bar{p}h_{\max} - A_1 U(h_{\max}). \tag{3.32}$$

Substituting (3.31) and $h_{\max} \sim \frac{1}{2}\bar{p}s^2$ into (3.32), we obtain

$$h'(s) = -\sqrt{\bar{p}^2 s^2 - \frac{A_1}{3}}\left(1 + \frac{A_1}{2A_2}\right) + O(\varepsilon) + O(\varepsilon/A_2). \tag{3.33}$$

This shows how the limiting contact angle is approached as the wettability ratio, A_2/A_1, is increased; see Fig. 12(b). We note that this value is lowered by wettability effects (as represented by the $A_1/3$ term) relative to the contact angle of large drops (3.14) or confined drops (3.19) where the locally

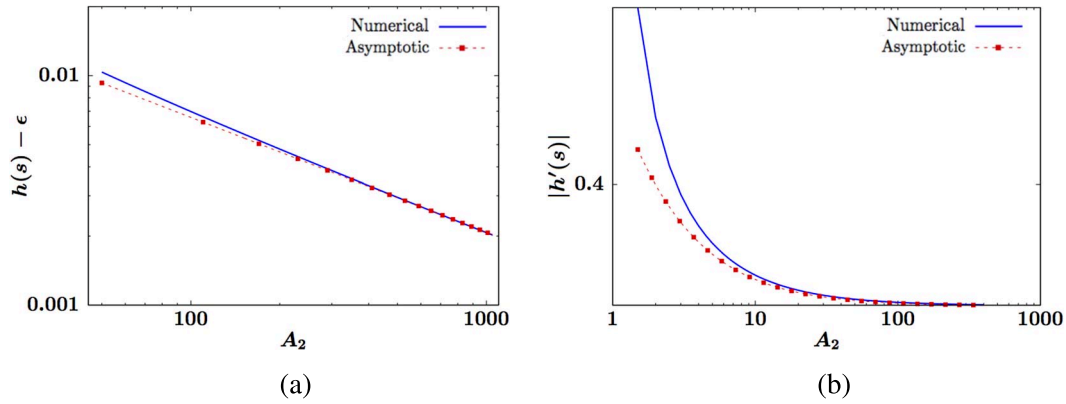

FIG. 12. Properties of branch 3 pinned droplet solutions computed with parameter values $A_1 = 1$, $L = 6$, $s = 3$, $\varepsilon = 0.1$. (a) Comparison of $h(s) - \varepsilon$ computed numerically with $\bar{p} = 0.292$ (blue) and from the asymptotic approximation (3.31) (red dots) for large A_2 plotted on log scale. (b) The contact angle $|h'(s)|$ vs. A_2 with fixed pressure $\bar{p} = 0.22$, plotted on log scale, the numerical result (blue) compared with the asymptotic prediction (3.33) (red dots).

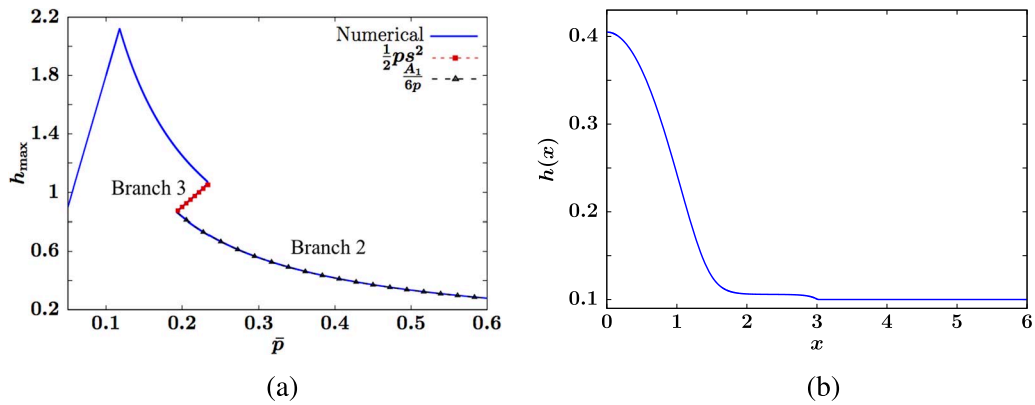

FIG. 13. Small and pinned droplets. (a) The bifurcation diagram for $\bar{p}$ vs. $h_{\max}$ highlighting branches 2 and 3. The solid blue curve gives numerical results. The black and red dotted curves represent the asymptotic prediction of $h_{\max}$ for branch 2 and branch 3 solutions, respectively, in the limit $\varepsilon \to 0$, with parameters $A_1 = 1$, $A_2 = 1.5$, $L = 6$, $s = 3$, $\varepsilon = 0.001$. (b) Profile of a steady state on branch 2, characterized by a droplet on $[0, s]$ and nearly uniform thin film on $[s, L]$.

homogeneous (A_2) wetting properties or the boundary conditions, respectively, set the contact angle. At the other edge of the pressure-range for this branch, the vanishing contact angle predicted by (3.33) is lower than what would be expected for small droplets ($|h_x| \sim \sqrt{A_1/3}$) because in this limit, the pinning effect is weaker and the effective width decreases from the position of the wetting heterogeneity, $w < s$.

The asymptotic prediction $h_{\max} \sim \frac{1}{2}\bar{p}s^2$, represented by the red dotted curve in Fig. 13 is compared with the numerically computed bifurcation curve. We observe that the leading-order asymptotic prediction agrees well with the numerical results.

3.4 *Small-width droplets*

Finally, we conclude with branch 2, whose solutions combine features from both droplets and nearly flat films. This branch describes small droplets with an effective width smaller than the size of the hydrophilic domain, $w < s$, and a surrounding nearly flat film that covers the remainder of the domain; see Fig. 13(b).

Branch 2 folds back from branch 1 in Fig. 4(b) giving droplets whose cores completely reside in the A_1 region. Compared with branch 1 solutions which are thin, nearly flat films over the entire domain, in the outer A_1 and A_2 regions and a boundary layer near $x = s$, solutions on branch 2 are characterized by larger mass so that droplets could form on the A_1 region, but not so large as to yield branch 3 or 4 type droplets that fill or extend beyond the A_1 region (having widths $w \geqslant s$). This class of solutions has the smallest mass possible for droplets centred at $x = 0$.

We construct the solution in the limit $A_2 \to \infty$ with A_1 fixed. On the A_2 region, the same matched asymptotics used for branch 3, (3.26) and (3.28), similarly yields the solution as (3.27) and (3.29) with $h(s) = \varepsilon + O(\delta^{1/2})$, but we must use a different argument to determine C_2.

To find C_2 in (3.29), we consider the steady state on the A_1 region. To leading order as $\delta \to 0$, the steady-state problem for $h \sim h_0(x)$ on $0 \leqslant x \leqslant s$ is given by

$$\frac{d^2h_0}{dx^2} = A_1\Pi(h_0) - \bar{p} \tag{3.34a}$$

$$h_0'(0) = 0, \qquad h_0(s) = \varepsilon. \tag{3.34b}$$

Noting that the boundary condition $h_0(s) = \varepsilon$ is less than the saddle point $h = H_{s,1}$, the trajectory for $h_0(x)$ must lie outside the A_1-homoclinic orbit in the phase plane. Since the solution is monotone decreasing with $h(0) = O(1)$, there must be a point x_1 with $0 < x_1 < s$ where $h_0(x_1) = H_{s,1}$. This will be a non-stationary inflection point of the solution. Linearizing (3.34a) about $H_{s,1}$ and using $\varepsilon \ll 1$ the solution on $x_1 < x \leqslant s$ can be approximated by

$$h(x) \approx H_{s,1} - C_1 e^{\sqrt{A_1\Pi'(H_{s,1})}\,(x-s)}. \tag{3.35}$$

Applying boundary conditions (2.9) to (3.35) and (3.29) yields

$$C_1 = \frac{H_{s,1} - \varepsilon}{\varepsilon\sqrt{\delta}\sqrt{A_1\Pi'(H_{s,1})} + 1}, \qquad C_2 = \frac{\varepsilon\sqrt{A_1\Pi'(H_{s,1})}\,(H_{s,1} - \varepsilon)}{\varepsilon\sqrt{\delta}\sqrt{A_1\Pi'(H_{s,1})} + 1}. \tag{3.36}$$

If we take $\varepsilon \to 0$ and $\delta \to 0$, to leading order we get $C_2 \sim \frac{\varepsilon^2\bar{p}}{\sqrt{A_1}}$ and thus

$$h(s) \sim \varepsilon + \frac{\varepsilon^2\bar{p}}{\sqrt{A_1A_2}}. \tag{3.37}$$

This resembles the H_s saddle value with an effective wetting coefficient given by the geometric mean of A_1 and A_2 and remains less than $H_{s,1} \sim \varepsilon + \varepsilon^2\bar{p}/A_1$ since $A_2 > A_1$.

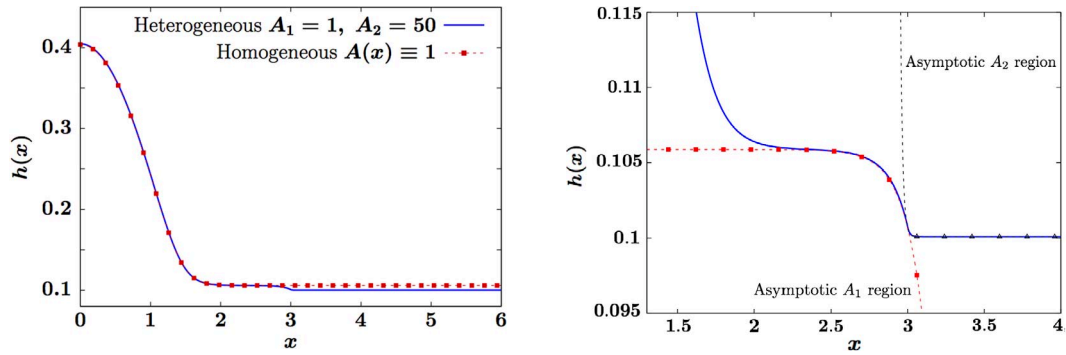

(a) (b)

FIG. 14. Details for a branch 2 solution computed with parameters $L = 6$, $s = 3$, $A_1 = 1$, $A_2 = 50$, $\varepsilon = 0.1$, $\bar{p} = 0.467$. (a) Comparison of the numerical solution (blue) on the heterogeneous substrate with its corresponding A_1-homogeneous homoclinic (red dots) with the same pressure. (b) Comparison of the numerically computed steady-state (blue) and the approximations ((3.35),(3.29)) for the structure near the interface $x = s$ (red, black dots).

Noting (3.37) and (3.27) motivates writing (2.15) as

$$A_1 U(h(s)) + \bar{p} h_{\max} = \bar{p} h_{\min} + A_1 U(h_{\max}) + A_2 \left(U(h(s)) - U(h_{\min}) \right), \tag{3.38}$$

where if $h_{\max} = O(1)$ then three terms on the right are each $O(\varepsilon)$ or smaller. Consequently balancing terms on the left, at leading order, we get $h_{\max} \sim A_1/(6\bar{p})$ for $\varepsilon \to 0$. This is the leading-order approximation of the maximum film thickness of the A_1-homoclinic (which can be obtained by solving $R_1(H_{s,1}) = 0$). This suggests that as $A_2 \to \infty$, the droplet core on $0 \leqslant x < x_1 < s$ can be approximated to leading order by the A_1-homoclinic solution on $0 \leqslant x < x_1 < s$. Figure 14 shows the profile of a branch 2 solution for $A_2 = 50$; in Perazzo *et al.* (2017), this was called a 'D1' solution. Figure 14(a) shows a comparison with the A_1-homoclinic solution having the same pressure $\bar{p}$. Figure 14(b) shows (3.35) and (3.29) compared with the numerical solution on a heterogeneous substrate near the interface of A_1 and A_2 regions, $x = s$; similarly to the form of the branch 1 solutions (3.3). We note that some of these approximations break down for $\bar{p}$ near $p_{\max}$, where $h_{\max} = O(\varepsilon)$ and $U(h_{\max})$ in (3.38) is $O(1)$.

Figure 15 shows a schematic phase plane for a branch 2 solution (black curve) compared with the homoclinic orbits for the A_1-homogeneous and A_2-homogeneous problems (blue and red curves, respectively). From the arguments connecting to (3.34a), we know that $h_{\max} > H_{\max,1}$ and the branch 2 solution lies outside the A_1-homoclinic orbit for $h \geqslant h(s)$. From the fact that $h_{\min} > H_{s,2}$ for any finite L, we know that the solution must lie within the A_2-homoclinic for $h \leqslant h(s)$. The branch 2 solutions have two inflection points in the droplet tail, at heights $h = H_{s,1}$ and $h = h(s)$, giving them a characteristic 'staircase' or 'precursor-foot' appearance; see Fig. 14.

We also note that corresponding results can also be obtained in the limit $\varepsilon \to 0$ with fixed $A_2 = O(1)$; see Liu (2019). In particular, for $\varepsilon \to 0$, we can use the parabolic profile (3.10) to approximate the droplet portion of branch 2 solutions. Then, following similar form (3.11) for large drops, we can estimate the effective width of the core from $h_{\max}$ to yield $w \sim \sqrt{A_1/(3\bar{p}^2)}$. Branch 2 joins branch 3 when the 'small' drops attain maximum size as minimal pinned drops with $w \sim s$. This yields $\bar{p}^*_{2,3} \sim$

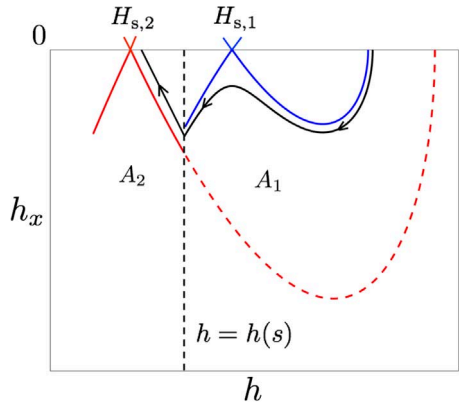

FIG. 15. Schematic of the lower half of the phase plane diagram showing the monotone decreasing portions of the homoclinic orbits for $A(x) \equiv A_1$ (blue) and $A(x) \equiv A_2$ (red) and the trajectory for a branch 2 solution.

$\sqrt{A_1/(3s^2)}$, corresponding to (3.25). Figure 13(a) shows the bifurcation diagram $h_{\max}$ vs. $\bar{p}$ zoomed into a portion of branches 2 and 3, computed numerically and asymptotically in the limit of small ε.

3.5 *Summary of the steady-state branches*

In examining the six branches, we have seen that each type of solution is impacted somewhat differently by the presence of the heterogeneous wetting. Distinct from groupings by droplets or film-like states, we can fundamentally separate the solutions into two sets based on phase plane structure.

- Solutions on branches 1 and 2 are given by trajectories from Fig. 15. They are characterized by having the height at the wetting interface fall between the saddles, $H_{s,2} < h(s) < H_{s,1}$ (for $\bar{p} < 0$ the order of the saddles is reversed). Portions of these solutions follow the stable and unstable manifolds from the $H_{s,1}$ and $H_{s,2}$ saddle points.
- Solutions on branches 3, 4, 5 and 6 are given by trajectories from Fig. 8. Here, the height at the switching point lies above both saddles, $h(s) > H_{s,1} > H_{s,2}$ with branches 4, 5 and 6 having $h(s) = O(1)$ and branch 3 with $h(s) = O(\varepsilon)$.

The pinned droplets, branch 3, transitions between these two cases at the $\bar{p}^*_{2,3}$ end, where $h(s)$ crosses $H_{s,1}$. For fixed A_1, A_2, the existence of turning points in Fig. 13(a) that define the range of pressures for this branch, (3.25), depends on ε being sufficiently small.

4. Leakage in the limit of large A_2

In the limit of large A_2, the A_2 region effectively becomes increasingly hydrophobic and should give a stronger confining effect on fluid in the A_1 region. This behaviour holds only for a range of small fluid masses, as wetting effects cannot be expected to influence thick layers of fluids. In terms of the six branches of steady-state solutions we have analysed, branches 2 and 3 described small and pinned drops that are effectively confined to the A_1 region. From (3.13) with $\bar{p}^*_{3,4} = \sqrt{A_2/(3s^2)}$, we obtain that

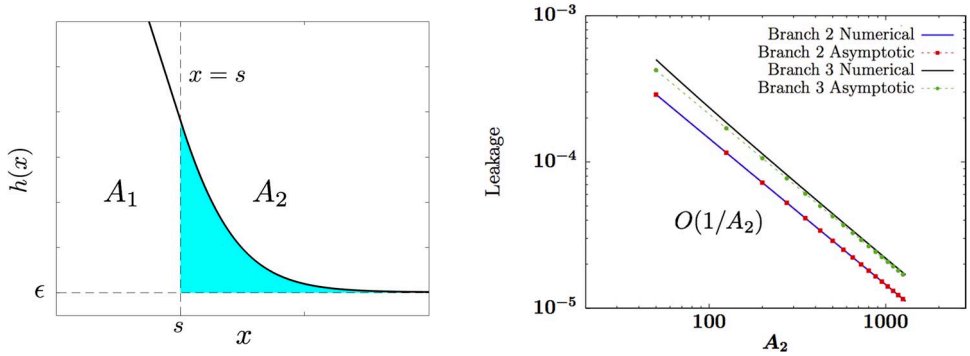

FIG. 16. (a) Schematic illustration of fluid leakage (4.2). (b) Leakage as a function of A_2 computed numerically and asymptotically for a branch 2 solution with $\bar{p} = 0.466$ and a branch 3 solution with $\bar{p} = 0.38$ plotted in log scale. The asymptotic prediction for branches 2 and 3 is given by (4.4) and (4.5), respectively. The pressure $\bar{p}$ is fixed as A_2 increases with $L = 6$, $s = 3$, $A_1 = 1$, $\varepsilon = 0.1$.

the maximum droplet mass that can be confined in the A_1 region is

$$m^*_{3,4} \sim \frac{s^2 A_2^{1/2}}{3\sqrt{3}}. \tag{4.1}$$

Note that this mass increases when the width of the A_1 region (s) is increased or A_2 is increased. In applications where accurate distribution of fluid on solid surfaces are required, it is important to develop a quantitative understanding of the degree of leakage or 'spillover' of the fluid from the A_1 region into the A_2 region. In this section, we present a measure of leakage for branch 2 and 3 solutions and show the leakage is inversely proportional to A_2.

In Sections 3.3 and 3.4, we showed that the film thickness at the heterogeneous interface is $h(s) \sim \varepsilon$ as $A_2 \to \infty$; see (3.31) and (3.37). We also showed that in the outer A_2 region, $h(x) \sim \varepsilon$ for $x > s$. To measure the fluid leakage, we use the fluid mass above $h(x) = \varepsilon$ on $x \in [s, L]$, as illustrated by the shaded region in Fig. 16(a).

We define the mass of leakage as

$$\text{Leakage} = \int_s^L \big[h(x) - \varepsilon\big]\, \mathrm{d}x. \tag{4.2}$$

Recalling (3.29), we can approximate the solution on $s \leqslant x \leqslant L$ as

$$h(x) \sim h_{\min,2} + \delta^{1/2} C_2 e^{-(x-s)/(\varepsilon\delta^{1/2})}. \tag{4.3}$$

Using earlier results, (3.27), we have $h_{\min,2} \sim \varepsilon + \delta\varepsilon^2\bar{p}$. For branch 2 solutions, from (3.36), $C_2 \sim \varepsilon^2\bar{p}/\sqrt{A_1}$ and this gives

$$\text{Leakage}_2 \sim \left(L - s + \frac{\varepsilon}{\sqrt{A_1}}\right)\frac{\varepsilon^2\bar{p}}{A_2}, \tag{4.4}$$

which gives that at the leading order, the fluid leakage of solutions on branch 2 is inversely proportional to A_2 for large A_2. Similarly, for branch 3 solutions, we use (3.31) to obtain

$$\text{Leakage}_3 \sim \left(L - s + \sqrt{s^2 - \frac{A_1}{3\bar{p}^2}}\right)\frac{\varepsilon^2\bar{p}}{A_2}. \tag{4.5}$$

Figure 16(b) shows the fluid leakage computed numerically and compared with the asymptotic estimate for solutions on branches 2 and 3 at fixed pressure over a range of A_2, plotted in log scale. The numerical result is obtained by first numerically solving for $h(x)$ and then numerically integrating (4.2) using the trapezoidal rule.

5. Axisymmetric steady-state solutions

We can extend our results for 1D thin films on heterogeneous substrates presented in Section 3 to axisymmetric solutions on 2D heterogeneous substrates with axisymmetric patterning.

For an axisymmetric film $h(r,t)$ on $0 \leqslant r \leqslant L$, the evolution (2.3a) takes the form

$$\frac{\partial h}{\partial t} = \frac{1}{r}\frac{\partial (rJ)}{\partial r} \qquad \text{with} \qquad J = h^3\frac{\partial}{\partial r}\left[A(r)\Pi(h) - \frac{1}{r}\frac{\partial}{\partial r}\left(r\frac{\partial h}{\partial r}\right)\right], \tag{5.1a}$$

where $J \equiv h^3\partial p/\partial r$ is the radial mass flux. Analogous to (2.3b), the boundary conditions needed at $r = 0$ for a smooth axisymmetric solution and at $r = L$ for no-meniscus and no-flux conditions are

$$\frac{\partial h}{\partial r}(0,t) = 0 \qquad \frac{\partial^3 h}{\partial r^3}(0,t) = 0, \qquad \frac{\partial h}{\partial r}(L,t) = 0 \qquad J(L,t) = 0, \tag{5.1b}$$

and we enforce conditions (2.9a) and (2.9b) on the smoothness of solutions at the jump in substrate wetting properties, $r = s$. The mass of the axisymmetric solutions $h(r;\bar{p})$ is given by $m = 2\pi\int_0^L hr\,\mathrm{d}r$ and the average film height is $\bar{h} = 2\int_0^L hr\,dr/L^2$.

The positive steady states for this problem are still be parametrized by a uniform pressure $p \equiv \bar{p}$. It follows that the steady-state axisymmetric solutions on $0 \leqslant r \leqslant L$ satisfy

$$\frac{1}{r}\frac{d}{dr}\left(r\frac{dh}{dr}\right) = A(r)\Pi(h) - \bar{p} \tag{5.2a}$$

$$h'(0) = 0 \qquad h'(L) = 0. \tag{5.2b}$$

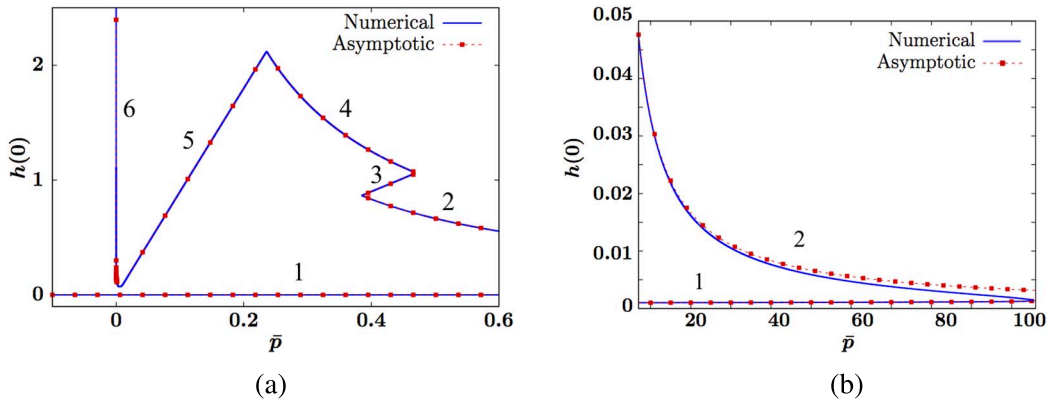

FIG. 17. Bifurcation diagram for $h(0) = h_{\max}$ vs. $\bar{p}$ for (a) small $\bar{p}$. (b) large $\bar{p}$. The solid curve denotes the numerically computed bifurcation curve. The dashed and dotted curve denotes the asymptotic prediction of $h_{\max}$ derived for each branch in the limit of small ε. In both (a) and (b), $A_1 = 1$, $A_2 = 1.5$, $L = 6$, $s = 3$, $\varepsilon = 0.001$.

Directly corresponding to (2.1), we take the coefficient of the disjoining pressure to describe an axisymmetrically patterned substrate,

$$A(r) = \begin{cases} A_1 & 0 \leqslant r \leqslant s, \\ A_2 & s < r \leqslant L. \end{cases} \tag{5.3}$$

Consequently, the axisymmetric equivalent of (2.15) is given by

$$(A_2 - A_1)U(h(s)) = A_2 U(h_{\min}) - A_1 U(h_{\max}) + \bar{p}(h_{\max} - h_{\min}) - \int_0^L \frac{h'^2}{r}\,\mathrm{d}r. \tag{5.4}$$

Since (5.2a) is not a piecewise-autonomous equation, the phase plane arguments described in Section 3 do not carry over, but we find that most of the other ideas in the asymptotic constructions do apply similarly. The steady-state axisymmetric solutions separate into six different branches directly corresponding to the six branches found in Section 3 for one dimension; see Fig. 17. Here, we will briefly identify the key steps needed to obtain the axisymmetric solutions and highlight results that we will use further.

5.1 *Small-thickness and large-thickness nearly flat films*

As in Section 3.1, steady nearly flat solutions generated by the jump in wetting properties can be described by linearizing (5.2a).

For very thin films, the disjoining pressure will balance the uniform pressure, $A_i \Pi(h) = \bar{p}$, to set piecewise constant heights, $H_{s,i}$, as in (3.1). Linearizing about these yields a piecewise-defined modified Bessel equation of order zero,

$$h_1'' + \frac{1}{r}h_1' = \begin{cases} A_1 \Pi'(H_{s,1})h_1 & 0 \leqslant r \leqslant s, \\ A_2 \Pi'(H_{s,2})h_1 & s < r \leqslant L. \end{cases} \tag{5.5}$$

Consequently, axisymmetric branch 1 solutions can be approximated by

$$h(r) \approx \begin{cases} H_{s,1} + C_1 I_0\left(\sqrt{A_1 \Pi'(H_{s,1})}\, r\right) & 0 \leqslant r \leqslant s, \\ H_{s,2} + C_2 K_0\left(\sqrt{A_2 \Pi'(H_{s,2})}\, r\right) & s < r \leqslant L, \end{cases} \tag{5.6}$$

where $I_0(r)$ and $K_0(r)$ are modified Bessel functions of the first kind and second kind, respectively. C_1 and C_2 are constants to be determined by enforcing the continuity and smoothness of the solution at $r = s$.

For thick films, the disjoining pressure has a weaker influence and the solution can be linearized around a mean height $\bar{h} \gg O(\varepsilon)$. In the limit $\bar{h} \to \infty$ (having $\Pi'(\bar{h}) < 0$), the linearized problem is a regular Bessel equation of order zero, and we can write the axisymmetric branch 6 solutions as

$$h(r) \sim \begin{cases} \bar{h} + C_1 J_0\left(\sqrt{-A_1 \Pi'(\bar{h})}\, r\right) - \frac{A_1 \Pi(\bar{h}) - \bar{p}}{A_1 \Pi'(\bar{h})} & 0 \leqslant r \leqslant s \\ \bar{h} + C_2 J_0\left(\sqrt{-A_2 \Pi'(\bar{h})}\, r\right) + C_3 Y_0(\sqrt{-A_2 \Pi'(\bar{h})}\, r) - \frac{A_2 \Pi(\bar{h}) - \bar{p}}{A_2 \Pi'(\bar{h})} & s < r \leqslant L, \end{cases} \tag{5.7}$$

where $J_0(r)$ and $Y_0(r)$ are Bessel functions of the first and second kinds with constants C_1, C_2 and C_3 to be determined by the continuity conditions at $r = s$ and the boundary condition at $r = L$. To determine $\bar{p}$, we use that (5.7) must satisfy the condition $\int_0^L hr\, dr = \bar{h}L^2/2$. In the limit $\bar{h} \to \infty$, this yields

$$\bar{p} \sim \left(A_1 \frac{s^2}{L^2} + A_2 \frac{L^2 - s^2}{L^2}\right) \frac{\varepsilon^2}{\bar{h}^3} + O\left(\frac{\varepsilon^3}{\bar{h}^4}\right), \tag{5.8}$$

like (3.7), this pressure is an area-weighted average of the disjoining pressure between the hydrophilic and hydrophobic regions (5.3).

5.2 *Droplet-type axisymmetric solutions*

As was the case for one dimension, for axisymmetric droplet solutions are primarily characterized by a core region where $h = O(1)$ as $\varepsilon \to 0$. In the core, to leading order, the uniform pressure balances surface tension with the disjoining pressure being negligible,

$$\frac{d}{dr}\left(r \frac{dh}{dr}\right) \sim -\bar{p} r. \tag{5.9}$$

This yields a parabolic profile analogous to (3.10) but with a modified coefficient,

$$h(r) = h_{\max} - \frac{1}{4}\bar{p} r^2 + O(\varepsilon), \tag{5.10}$$

and $h = O(\varepsilon)$ outside the core. The width w, where $h(w) = O(\varepsilon)$, now represents the effective radius of the core,

$$w \sim \sqrt{\frac{4h_{\max}}{\bar{p}}}, \tag{5.11}$$

and (5.10) can also be written as $h \sim \frac{1}{4}\bar{p}(w^2 - r^2)$ yielding a mass $m \sim 2\pi h_{\max}^2/\bar{p}$; see also Glasner *et al.* (2009). What remains to define the different branches of droplet solutions is to make use of information on the contact line position and the far-field of the droplet through (5.4).

Using (5.10) and (5.11), we can approximate the integral term in (5.4) as

$$\int_0^L \frac{h'(r)^2}{r}\,\mathrm{d}r \sim \int_0^w \frac{h'(r)^2}{r}\,\mathrm{d}r \sim \int_0^w \frac{1}{4}\bar{p}^2 r\,\mathrm{d}r \sim \frac{1}{2}\bar{p}h_{\max}.$$

Consequently, (5.4) for droplet solutions can be approximated by

$$(A_2 - A_1)U(h(s)) = A_2 U(h_{\min}) - A_1 U(h_{\max}) + \frac{1}{2}\bar{p}h_{\max} - \bar{p}h_{\min}, \tag{5.12}$$

then the axisymmetric droplet solutions follow using analogous arguments from Section 3.

- Branch 2: small radii droplets, $w < s$ with

$$h_{\max} \sim \frac{A_1}{3\bar{p}} \qquad w \sim \sqrt{\frac{4A_1}{3\bar{p}^2}} \qquad h(s) \sim \varepsilon \qquad \text{for} \qquad \bar{p} > \sqrt{\frac{4A_1}{3s^2}}.$$

- Branch 3: pinned droplets, $w \sim s$ with

$$h_{\max} \sim \frac{1}{4}\bar{p}s^2 \qquad h(s) \sim \varepsilon + \frac{\varepsilon}{\sqrt{A_2}}\sqrt{\frac{1}{4}\bar{p}^2 s^2 - \frac{A_1}{3}} \qquad h'(s) \sim -\sqrt{\frac{1}{4}\bar{p}^2 s^2 - \frac{A_1}{3}}$$

  for $\sqrt{4A_1/(3s^2)} < \bar{p} < \sqrt{4A_2/(3s^2)}$. Note that these results differ from the 1D results (3.31) and (3.33) only by a coefficient and the contact angle is lowered relative to estimate based on the droplet core, $|h'(w)| \sim \frac{1}{2}\bar{p}w$.

- Branch 4: large radii droplets, $s < w < L$ with

$$h_{\max} \sim \frac{A_2}{3\bar{p}} \qquad w \sim \sqrt{\frac{4A_2}{3\bar{p}^2}} \qquad \text{for} \qquad \sqrt{\frac{4A_2}{3L^2}} < \bar{p} < \sqrt{\frac{4A_2}{3s^2}}.$$

  on $\sqrt{4A_2/(3L^2)} < \bar{p} < \sqrt{4A_2/(3s^2)}$.

- Branch 5: confined droplets, $w \sim L$ with

$$h_{\max} \sim \frac{1}{4}\bar{p}L^2 \qquad h'(L) \sim -\frac{1}{2}\bar{p}L \qquad \text{for} \qquad \bar{p} < \sqrt{\frac{4A_2}{3L^2}}.$$

Figure 17(a and b) show the bifurcation diagram $h(0) = h_{\max}$ vs. $\bar{p}$ computed for small and large $\bar{p}$, respectively, compared with the asymptotic estimates given above.

6. Stability of the steady-state solutions

Here, we apply linear stability analysis to the 1D steady-state solutions described in Section 3. Writing the steady states as $h_*(x) = h(x;\bar{p})$, we express perturbed solutions as $h(x,t) = h_*(x) + \delta h_1(x,t)$ for $\delta \ll 1$. Plugging into the evolution (2.3a) and linearizing, at $O(\delta)$, we obtain

$$\frac{\partial h_1}{\partial t} = \mathscr{L}_{h_*} h_1, \tag{6.1}$$

where the linear operator $\mathscr{L}_{h_*}$ is given by

$$\mathscr{L}_{h_*} g \equiv \frac{\partial}{\partial x}\left(h_*^3(x)\frac{\partial}{\partial x}\left[A(x)\Pi'(h_*)g - \frac{\partial^2 g}{\partial x^2}\right]\right) \tag{6.2a}$$

$$\frac{\partial g}{\partial x}(0,t) = 0 \qquad \frac{\partial^3 g}{\partial x^3}(0,t) = 0, \qquad \frac{\partial g}{\partial x}(L,t) = 0 \qquad \frac{\partial^3 g}{\partial x^3}(L,t) = 0. \tag{6.2b}$$

By separation of variables, we can write $h_1(x,t) = \sum_n c_n g_n(x) e^{\lambda_n t}$ where $(g_n(x), \lambda_n)$ are eigenmodes of

$$\mathscr{L}_{h_*} g = \lambda g. \tag{6.3}$$

Results from Laugesen & Pugh (2000a) and Bertozzi *et al.* (2001) provide guidance on interpreting the linear stability analysis. Since there are continuous branches of steady states, there will be a zero eigenmode corrresponding to perturbations of the mass; we will neglect this mode and consider only modes with zero-mean eigenfunctions. The steady state $h_*(x)$ is then linearly stable if all $\mathrm{Re}(\lambda_n) < 0$. It was shown in Laugesen & Pugh (2000a) that for the Neumann problem, steady states with critical points in the interior of the domain cannot be linearly stable. Periodic solutions and single droplets centred in the domain will have modes that are anti-symmetric with respect to the critical points. In the periodic case, there will be a neutrally stable translational mode, $g(x) = h_*'(x)$. There will also be unstable modes describing coarsening, where droplets merge and evolve to a solution with longer spatial period (see, e.g. Kargupta & Sharma, 2001; Thiele *et al.*, 2003). We will see that this ultimately leads to fluid accumulating at the edge of the domain as a stable large half-droplet.

We numerically investigate the linear stability of the six different branches of solutions discussed in Section 3 with typical parameters $A_1 = 1$, $A_2 = 50$, $L = 6$, $s = 3$, $\varepsilon = 0.1$. Second-order accurate finite-difference discretizations of the steady-state solutions of (2.11) are found by continuation in pressure $\bar{p}$ for all the six branches. Then, a discretized form of the linear operator (6.2a) can be obtained as a matrix. The eigenvalues of the linear stability problem (6.3) are then obtained using MATLAB's eigenvalue solver.

We find that branch 5 is the only unstable branch, while other branches all characterize stable steady-state solutions. We need to explain how this is consistent with the form of the diagram for $\bar{p}$ vs. $h_{\max}$ shown in Fig. 4(b). Although it appears that there are multiple turning points that imply changes in stability as the solution passes through these points, the only turning points associated with stability change are the points connecting branches 4 and 5 and connecting branches 5 and 6. It has been previously shown in Bertozzi *et al.* (2001) for thin films on homogeneous substrates that the mass m and the maximum film thickness $h_{\max}$ are the extrinsic parameters that determine the emergence

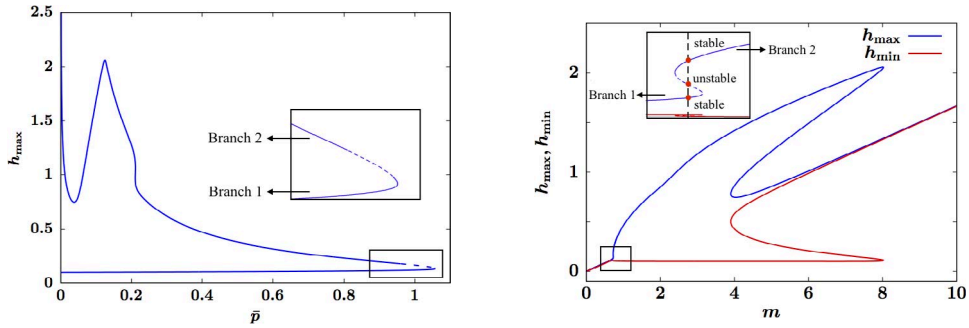

(a) (b)

FIG. 18. Bifurcation diagrams for parameters $L = 6$, $s = 3$, $A_1 = 1$, $A_2 = 1.5$, $\varepsilon = 0.1$: (a) bifurcation diagram for $\bar{p}$ vs. $h_{\max}$ (b) bifurcation diagram for m vs. $h_{\max}, h_{\min}$. The insets show the same range of solutions where branches 1 and 2 meet in terms of both bifurcation diagrams, with stability indicated in (b). The dashed segment denotes the unstable part of branch 2 in both bifurcation diagrams.

of bifurcations. The pressure $\bar{p}$ should be viewed as an intrinsic parameter that can be computed by $\bar{p} = \int_0^L \Pi(h_*(x))\,\mathrm{d}x/L$ once $h_*(x)$ is determined. Observe that in Fig. 4(b), viewed with respect to decreasing $h_{\max}$ from above, a saddle-node bifurcation occurs between branches 4 and 5, with branch 4 being the stable branch and branch 5 the unstable branch. If we increase $h_{\max}$ from below, another saddle-node bifurcation occurs at between branches 5 and 6, with branch 6 being the stable branch, which is consistent with the finding that branch 5 is the only unstable branch for the parameters used above. Also see the stability indicated in Fig. 3(c).

Depending on the choice of parameters, a part of branch 2 near the connection with branch 1 may also be unstable. Figure 18 shows bifurcation diagrams for $\bar{p}$ vs. $h_{\max}$ and m vs. $h_{\max}, h_{\min}$. The inset plot in Fig. 18(a) zooms into the end of branch 2 that connects with branch 1. This corresponds to the inset plot shown in Fig. 18(b), showing the same solution branches yield an S-shaped curve plotted using m vs. $h_{\max}, h_{\min}$, indicating saddle-node bifurcations. There is a small range of mass for which three different steady states exist with the same mass. Two of the steady states are branch 2 solutions. Of the two branch 2 solutions, the solution with the smaller amplitude is unstable. The third steady state is a branch 1 solution. The unstable part of branch 2 is represented by the dashed curve in Fig. 18. As will be discussed further, increasing A_2 has the effect of stabilizing branch 2 solutions. We found that for $L = 6$, $s = 3, \varepsilon = 0.1$ fixed, as A_2 increases, the unstable part of branch 2 vanishes.

It was shown that steady states on branch 5 are parametrized by a finite range of pressures $\bar{p}$. Corresponding to a finite range of masses, in Fig. 3(c) this is approximately $1.2 < m < 1.6$. Branches 4 and 6 are defined over the same range of masses, suggesting mass-conserving bi-stable dynamics of (2.3) separated by branch 5. Figure 19 confirms this description by showing the two different stable equilibria approached by the solution at large times starting from initial data given by a branch 5 solution with small perturbations of opposite sign. Figure 19(a) shows that when the initial condition is given by $h(x, 0) = h_*(x) + \delta g_1(x)$ where $g_1(x)$ is the unstable eigenmode of $h_*(x)$, the stable branch 6 solution is approached. In contrast, in Fig. 19(b) starting from the initial condition $h(x, 0) = h_*(x) - \delta g_1(x)$, the dynamics lead to the branch 4 solution with the same mass, $m \approx 12.8$.

In Section 2, we noted the existence of further branches of solutions in the bifurcation diagram, besides the primary (outer-most) loop (Fig. 4(b)) that we have been studying, for heterogeneous

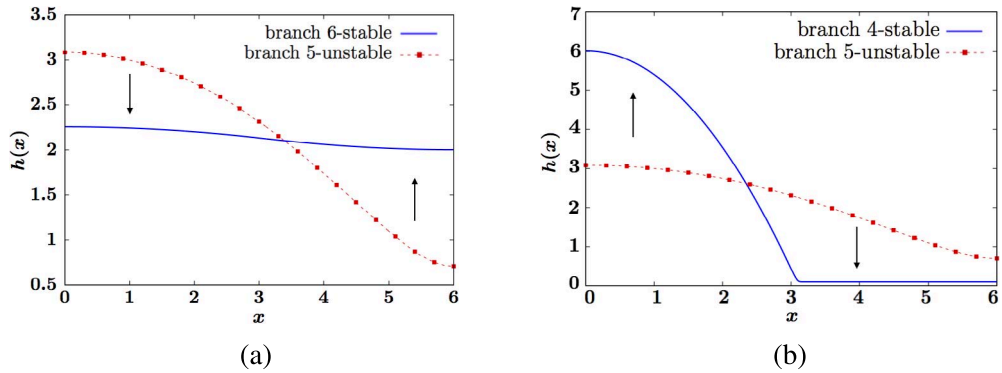

FIG. 19. Bi-stable dynamics with respect to perturbations of an unstable branch 5 solution $h_*(x)$. (a) Initial conditions (red dotted curve) $h(x,0) = h_*(x) + \delta g_1(x)$, with $g_1(x)$ being the unstable eigenmode of h_* and small $\delta > 0$, evolving to the stable branch 6 solution (blue curve). (b) Initial conditions $h(x,0) = h_*(x) - \delta g_1(x)$ evolving to the stable branch 4 solution.

substrates with sufficiently large domain size L. We use the values of the system parameters from Fig. 3(c) and consider the stability of solutions off the primary loop. We compute the eigenvalues for the four solutions with mass $m = 0.6$ marked by asterisks in the bifurcation diagram shown in Fig. 20(a). Figure 20(b) shows the corresponding profiles of the four solutions. Linear stability analysis suggests that of these four steady states, only solution d, which is a solution representing a large droplet centred at $x = L$ on the larger loop compared with the solutions a-c, is stable; solutions a-c are unstable. Specifically, solutions b and c have one unstable eigenvalue and solution a has two unstable eigenvalues, which is consistent with the observed fold points of the inner loop. At each fold point, the number of unstable eigenvalues changes by one, implying one eigenvalue crosses through zero. The dominant eigenvalue for solution d, $\lambda_1 \approx -0.065$, is smaller in amplitude compared with $\lambda_1 \approx -0.08$ for the stable droplet centred at $x = 0$. This suggests that while both droplets are stable to infinitesimal perturbations, the droplet in the hydrophilic region may be the attracting state for dynamics starting from most generic initial conditions at this mass. Such stability considerations led us to focus on the outer loop of solutions.

In Sections 3.3 and 4, we quantified the pinning effect of an increasing wettability contrast on branch 2 and 3 droplets. Here, we show that increasing A_2 can increase the relative stability of a branch 2 droplet at a fixed mass. Figure 21 shows the largest eigenvalue of a steady-state branch 2 droplet with mass $m = 3.5$ as a function of A_2. As A_2 increases, the leading eigenvalue λ_1 becomes more negative, making the steady state more stable with small perturbations decaying faster. We will see further influences of large A_2 on the dynamics in the next section.

7. Dynamics of 1D solutions

The dewetting dynamics of thin films on hydrophobic substrates involves many regimes starting from linear instabilities of perturbed films, leading to pattern formation and long-time breakup into droplets connected by thin precursor films; see, e.g. Thiele *et al.* (2001). An important step in showing that model (2.3) can represent these dynamics for homogeneous substrates ($A(x) \equiv 1$) was the proof in Bertozzi *et al.* (2001) that film thicknesses remain positive for all times. In the appendix here, we extend their

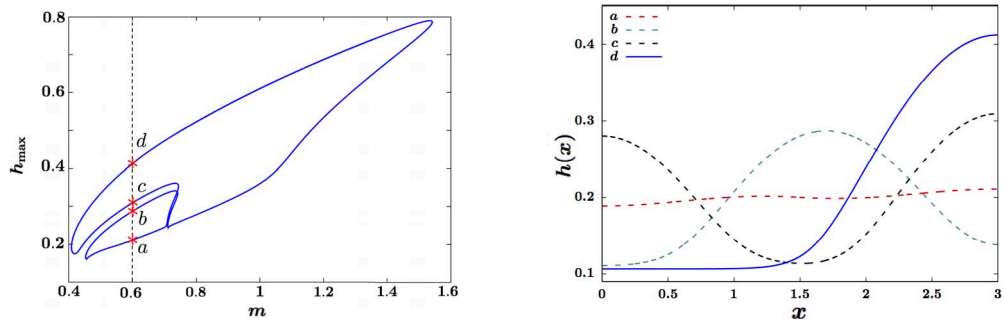

FIG. 20. (a) Part of the bifurcation diagram from Fig. 3(c) highlighting four distinct non-primary steady states with mass $m = 0.6$. (b) The corresponding height profiles of the four solutions, of which *a*-*c* were shown in Fig. 3(e) and *d* is a large droplet centred at $x = L$.

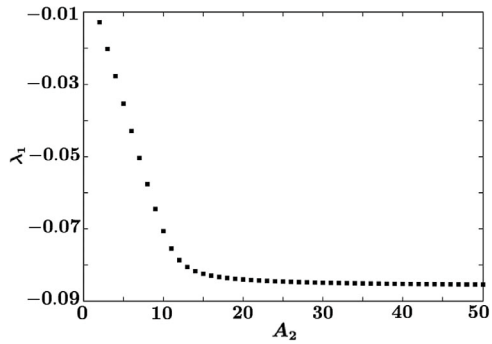

FIG. 21. The largest eigenvalue λ_1 of a steady-state branch 2 droplet with fixed mass on a substrate with increasing A_2 for parameters $m = 3.5, L = 10, s = 5, A_1 = 1, \varepsilon = 0.1$.

proof to apply to (2.3) with heterogeneous wetting given by (2.1). Given that result, here we briefly address the influence of heterogeneous wetting properties on the timescales of the dewetting dynamics.

Figure 22 compares the evolution of a thin film on substrates with homogeneous and heterogeneous wetting properties, (2.2) with $\varepsilon = 0.1$, on a domain with $L = 10$. The initial condition is given by a perturbed thin film $h(x, 0) = 0.35\left[1 + 0.1\cos\left(\frac{2\pi x}{L}\right) + 0.1\cos\left(\frac{3\pi x}{L}\right)\right]$ with mass $m = 3.5$. In each of three simulations, we illustrate the dynamics by showing the evolution of the height profiles as surface plots along with plotting the evolution of the energy (2.5).

On the homogeneous substrate, with $A(x) \equiv 1$ (Fig. 22(a)), the thin film de-stabilizes to form two droplets of different sizes centred at $x = 0$ and $x = L$. This is accompanied by a rapid decrease in the energy from the initial value. Thereafter, the drops slowly evolve. The droplet at $x = L$ slowly gains mass as time increases, eventually leading to an equilibrium with one large droplet centred at $x = L$.

Figure 22(b) shows the evolution starting from the same initial film on a stepwise-patterned substrate with $s = 5, A_1 = 1$ and $A_2 = 5$. While the film also breaks up to form two droplets in this case, the right droplet initially develops at an interior position, at some x_* with $s < x_* < L$. As time increases, the right droplet moves towards $x = L$ and loses mass, eventually leading to one single equilibrium

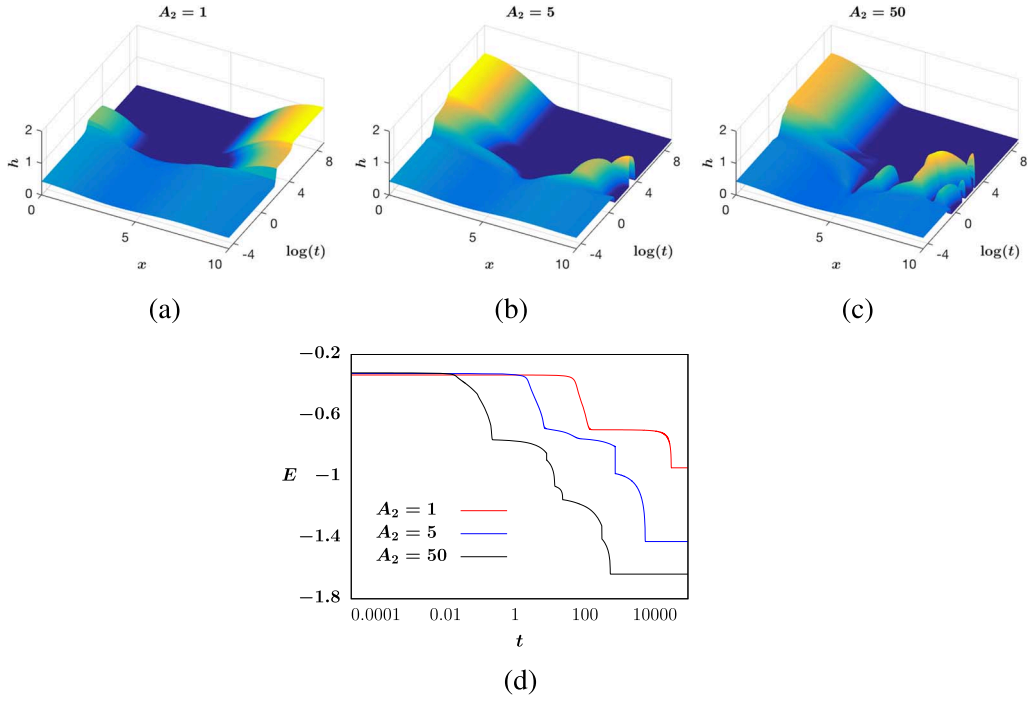

FIG. 22. Surface plots that demonstrate the dewetting dynamics of thin films over time starting from the same initial profile on $0 \leqslant x \leqslant 10$ with $\varepsilon = 0.1$ on (a) a homogeneous substrate with $A(x) \equiv 1$, (b) a heterogeneous substrate with $A_2 = 5$ on $5 \leqslant x \leqslant 10$ and (c) a heterogeneous substrate with $A_2 = 50$ on $5 \leqslant x \leqslant 10$. The time is plotted in log scale. (d) The corresponding energy given by (2.5) of the thin films over time on substrates described in (a,b,c).

droplet centred at $x = 0$. In this evolution, the energy of the thin film has two stages of rapid decrease, first forming two drops from the film followed by the movement of the interior droplet to the edge of the domain. The two edge droplets then slowly evolve until a single-drop equilibrium is approached, as shown in Fig. 22(b). Note that compared with the homogeneous substrate case, the final droplet formed on the other side of the domain, and the timescale to reach this near-equilibrium phase was reduced by a factor of five.

Figure 22(c) shows the evolution of the thin film profile on the patterned substrate with $A_2 = 50$. The evolution of the thin film goes through a similar dewetting process. However, the droplet formed at the right boundary has a smaller width compared with the $A_2 = 5$ case and the stages of dynamics occurred in a much shorter time-scale, as can be observed in Fig. 22(d). This is consistent with the stabilizing effect of increasing A_2 evidenced by the eigenvalue calculation shown earlier in Fig. 21. With this larger value of A_2, the influence of the heterogeneity is more clear. In the early stages, a pinned drop forms in the relatively hydrophilic region while coarsening dynamics proceed on the hydrophobic region. For long times the pinned drop slowly evolves to become a stable steady-state droplet centred at $x = 0$; since the width of this drop is within the hydrophilic region ($w < s$), this is a branch 2 solution. Further work is needed to better understand the significant influence of substrate heterogeneity on the overall timescales and dynamics of thin film evolution.

8. Steady-state thin films on 2D substrates

So far, we have mainly focused on solutions for the simple 1D and axisymmetric cases. However, the chemical patterning of surfaces used in many microfluidic applications is generally much more complicated; see, e.g. Darhuber *et al.* (2001), Darhuber & Troian (2005) and Kašpar *et al.* (2016). Here, we study thin films on 2D heterogeneous surfaces with square and stripe patterning and show that the cross-sections of some 2D steady-state solutions on such surfaces can be approximated by 1D and axisymmetric solutions.

The generalization of (2.3a) to two dimensions for the evolution of $h(x, y, t)$ is

$$\frac{\partial h}{\partial t} = \nabla \cdot \left(h^3 \nabla \left[A(x, y) \Pi(h) - \nabla^2 h \right] \right), \tag{8.1}$$

and steady states are characterized by having constant pressures, $p = \bar{p}$, yielding the semilinear elliptic partial differential equation problem

$$\bar{p} = A(x, y) \Pi(h) - \nabla^2 h. \tag{8.2}$$

Computationally, we obtain stable steady states by applying efficient numerical schemes for (8.1) (Witelski & Bowen, 2003) and evolving the solution to sufficiently long times starting from initial conditions over a range of masses.

As in the 1D and axisymmetric cases, we focus on the droplet solutions centred at the origin. First, we study drops on a heterogeneous substrate with a relatively hydrophilic A_1-square patch in the centre, surrounded by a relatively hydrophobic A_2 region on a square domain with the Hamaker coefficient modelled by

$$A(x, y) = \begin{cases} A_1 & 0 \leqslant x \leqslant s \text{ and } 0 \leqslant y \leqslant s, \\ A_2 & \text{otherwise.} \end{cases} \tag{8.3}$$

With this geometry, we can take advantage of four-fold symmetry to get the solutions in terms of computing just the first quadrant. Our expectations are that small droplets, whose core fits well inside the A_1 square should be close to axisymmetric, as should large drops that overflow the A_1 square but are not so large as to be strongly influenced by the confining effects of the finite domain size. These correspond to branches 2 and 4 of the axisymmetric solutions found in Section 5. Between these cases should be 2D pinned drops whose structure depends significantly on the shape of the hydrophilic region.

To quantitatively compare the computed solutions on this substrate with the axisymmetric steady-state solutions, we define a measure for the difference of $h = h(x, y)$ from being an axisymmetric form, $h = h(r)$, as

$$D \equiv \int_0^{L_y} \int_0^{L_x} \left| x \frac{\partial h}{\partial y} - y \frac{\partial h}{\partial x} \right|^2 \mathrm{d}x \, \mathrm{d}y. \tag{8.4}$$

Note that written in polar coordinates, $D = \left\| \frac{\partial h}{\partial \theta} \right\|_{L_2}^2$; hence if a solution is axisymmetric, then $D = 0$.

Figure 23 shows film mass $m = \iint h \, \mathrm{d}x \, \mathrm{d}y$ vs. D plotted on log scale over a range of fluid masses on a square hydrophilic patch (8.3) with $A_2/A_1 = 10$. Droplet-type solutions, represented by blue triangular data points, correspond to pinned and unpinned droplets similar to those studied in Sections 3.2 and 3.3.

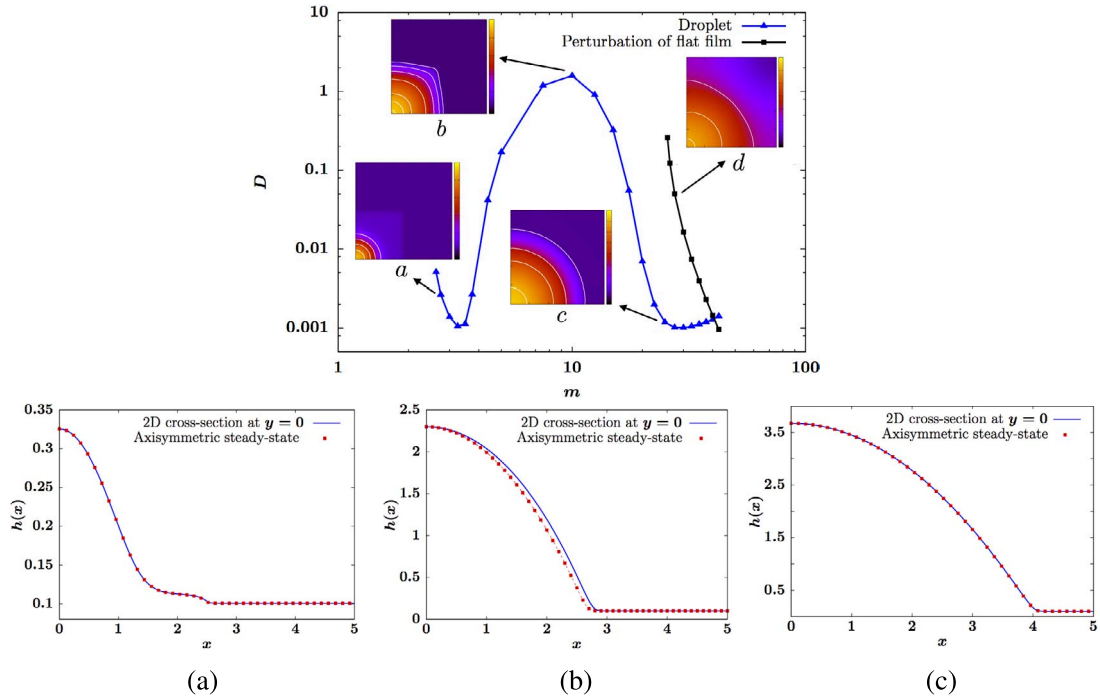

FIG. 23. Thin films on a hydrophilic square patch, $-s \leqslant x, y \leqslant s$: (top) Film mass m vs. D plotted in log scale for both droplet-type solutions and perturbations of thick flat films, with parameters $L = L_x = L_y = 5$, $A_1 = 1$, $A_2 = 10$, $s = L/2$. The insets show colour contour maps of four selected solutions (on one quarter of the domain, $0 \leqslant x, y \leqslant L$, reduced by symmetry). (a,b,c) Cross-section of the 2D solution at $y = 0$ compared with the axisymmetric steady-state solution with the same maximum film thickness for (a) droplet a (b) droplet b (c) droplet c. No cross-section profile is shown for the nearly uniform thick film marked by inset d.

We observe that the maximum D occurs at a pinned steady-state droplet with droplet width $w \approx s$. The contour map of the surface of the solution labelled b is also shown in Fig. 23. For solutions with mass larger than droplet b, the droplet becomes a large-radii unpinned droplet like a branch 4 solution, shown by the contour map labelled c. In this process, D gradually decreases. For masses smaller than droplet b, droplets gradually transition to being small-radii droplets like a branch 2 droplet with a smaller D, shown by the contour map of droplet a. Figure 23(a, b and c) confirms the excellent agreement of the computed solution with the axisymmetric height profiles for cases a, c and the noticeable difference with the anisotropic pinned droplet b. Above a certain mass, the wettability contrast is not strong enough to maintain droplets and the solution will take the form of a nearly uniform thick film. A branch of these solutions is also shown in the figure (indicated with black dots); as should be expected from earlier results for branch 6 solutions, the influence of the form of $A(x, y)$ decreases with increasing thickness.

Processes in many applications involve depositing liquids on periodic striped wettability patterns; see Ajaev *et al.* (2016), Brasjen *et al.* (2013), Honisch *et al.* (2015) and Kargupta & Sharma (2002). In particular, several different regimes for liquid droplets on substrates with stripe-like patterns have been identified in Honisch *et al.* (2015). Here, we show that depending on the regime, cross-sectional profiles of the 2D droplet can be predicted using the axisymmetric or 1D steady states. To simulate the

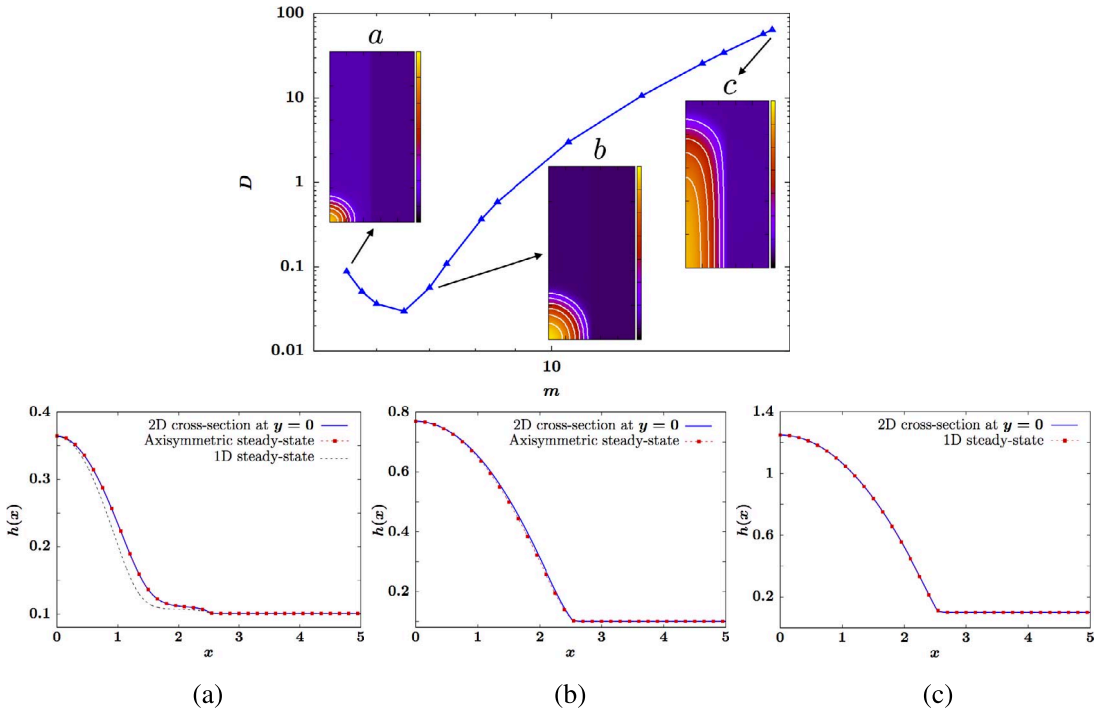

FIG. 24. Symmetric thin films on a hydrophilic stripe, $-s \leqslant x \leqslant s$: (top) Film mass m vs. D plotted in log scale for droplet-type solutions, with parameters $L_x = 5, L_y = 10, A_1 = 1, A_2 = 10, s = L_x/2$. The insets show colour contour maps of three selected solutions (on one quarter of the domain, reduced by symmetry). (a,b,c) Cross-sections of the 2D solutions at $y = 0$ compared with the axisymmetric and 1D steady states with the same maximum film thickness for droplets a, b, c, respectively.

deposition of liquids on a substrate with stripe-like patterns, we consider $A(x, y)$ of the form

$$A(x,y) = \begin{cases} A_1 & 0 \leqslant x \leqslant s, \\ A_2 & \text{otherwise.} \end{cases} \tag{8.5}$$

We focus on one-quarter of a droplet whose maximum film thickness occurs at $(0, 0)$, in the centre of the stripe. Figure 24 shows m vs. D plotted on log scale for droplets on striped substrates. When the fluid mass is small, with the droplet core fitting well inside the width of the stripe, the influence of the chemical heterogeneity on the droplets is limited. The droplets are closer to axisymmetric solutions with small D, as shown by the colour map of the surface of droplet a and droplet b highlighted in Fig. 24. As mass increases, the fluid grows in the y-direction and becomes increasingly non-axisymmetric, as shown by droplet c labelled in Fig. 24. Figure 24(a, b and c) show the cross-section of the 2D computed solution at $y = 0$ compared with the axisymmetric or 1D steady states with the same maximum film thickness for droplets a–c. We observe that the cross-section of droplet a and droplet b can be well approximated by the axisymmetric solution with the same maximum film thickness. As the fluid mass increases, D increases. The 1D steady state gives a better prediction of the cross-sectional profile at $y = 0$ for the elongated pinned droplet c.

9. Conclusions

This paper has considered the steady-state thin films on a finite chemically heterogeneous substrate with stepwise patterning. We have classified the primary steady-state solutions in one dimension into six different branches, for which we presented asymptotic analysis of solutions and have considered two limits, the small ε limit and the large wettability contrast limit. In particular, we investigated a new type of pinned droplet solutions that arise due to the heterogeneity of the substrate. We identified that an increasing A_2 has a confining effect on these pinned droplets. Through asymptotic analysis, we quantified the degree of confinement and leakage of fluid film in terms of the wettability contrast.

We showed that the results of the asymptotic analysis derived for 1D solutions can be directly extended to axisymmetric solutions. In addition, we discussed the stability of these steady-state solutions using linear stability analysis. We also extended a proof of positivity of solutions on homogeneous substrates to the case of heterogeneous substrates. Last, we explored the effect of heterogeneity on the dynamics of thin film evolution in one dimension and in square and striped geometries in two dimensions.

There are many interesting questions for further study suggested by this work. This includes analysing if the bifurcation structure of the six branches of solutions found for (2.2) holds for broader classes of $\Pi(h)$ disjoining functions and other forms for $A(x)$. More work is needed to study solutions on larger domains with periodic $A(x)$ functions, representing micro-arrays; it would be interesting to see if non-periodic steady states can exist. Similarly, understanding the structure of the higher-order branches in one dimension may be important for studies of dewetting. We hope that more use of the 1D and axisymmetric can be made for approaches to systematically approximate solutions of the 2D elliptic problem (8.2) in simple geometries like those studied in Brasjen & Darhuber (2011) and Brasjen *et al.* (2013). Further work is needed to compare our results for branch 3 pinned drops with the results for pinned drops on square patches given in Kašpar *et al.* (2016). Comparisons with studies of Stokes flows on pattern substrates (Asgari & Moosavi, 2012; Moosavi *et al.*, 2008) could shed light on limitations for using of thin film models with discontunuous wetting properties. Much more work is also needed to better understand the influence of heterogeneous wetting on dewetting and coarsening dynamics on larger domains as in Brusch *et al.* (2002), Thiele *et al.* (2003) and Asgari & Moosavi (2012).

Funding

National Science Foundation (NSF DMS 2008255 to T.W.).

References

Ajaev, V. S., Gatapova, E. Y. & Kabov, O. A. (2016) Stability and break-up of thin liquid films on patterned and structured surfaces. *Adv. Colloid Interface Sci.*, **228**, 92–104.

Asgari, M. & Moosavi, A. (2012) Coarsening dynamics of dewetting nanodroplets on chemically patterned substrates. *Phys. Rev. E (3)*, **86**, 016303.

Bertozzi, A. L., Grün, G. & Witelski, T. P. (2001) Dewetting films: bifurcations and concentrations. *Nonlinearity*, **14**, 1569–1592.

Bhushan, B., Jung, Y. C., Niemietz, A. & Koch, K. (2009) Lotus-like biomimetic hierarchical structures developed by the self-assembly of tubular plant waxes. *Langmuir*, **25**, 1659–1666.

Bliznyuk, O. (2011) Directional wetting on patterned surfaces. *Ph.D. Thesis*. Enschede, Netherland: University of Twente.

Brasjen, B. J. & Darhuber, A. A. (2011) Dry-spot nucleation in thin liquid films on chemically patterned surfaces. *Microfluid. Nanofluidics*, **11**, 703–716.

Brasjen, B. J., Gu, H. & Darhuber, A. A. (2013) Dewetting of thin liquid films on chemically patterned substrates: front propagation along narrow lyophobic stripes and stripe arrays. *Microfluid. Nanofluidics*, **14**, 669–682.

Brusch, L., Kühne, H., Thiele, U. & Bär, M. (2002) Dewetting of thin films on heterogeneous substrates: pinning versus coarsening. *Phys. Rev. E (3)*, **66**, 011602.

Craster, R. & Matar, O. (2009) Dynamics and stability of thin liquid films. *Rev. Modern Phys.*, **81**, 1131.

Darhuber, A. A. & Troian, S. M. (2005) Principles of microfluidic actuation by modulation of surface stresses. *Annu. Rev. Fluid Mech.*, **37**, 425–455.

Darhuber, A. A., Troian, S. M., Miller, S. M. & Wagner, S. (2000) Morphology of liquid microstructures on chemically patterned surfaces. *J. Appl. Phys.*, **87**, 7768–7775.

Darhuber, A. A., Troian, S. M. & Reisner, W. W. (2001) Dynamics of capillary spreading along hydrophilic microstripes. *Phys. Rev. E (3)*, **64**, 031603.

Dong, H., Carr, W. W. & Morris, J. F. (2006) Visualization of drop-on-demand inkjet: drop formation and deposition. *Rev. Sci. Instrum.*, **77**, 085101.

Glasner, K., Otto, F., Rump, T. & Slepčev, D. (2009) Ostwald ripening of droplets: the role of migration. *European J. Appl. Math.*, **20**, 1–67.

Glasner, K. B. (2003) Spreading of droplets under the influence of intermolecular forces. *Phys. Fluids*, **15**, 1837–1842.

Glasner, K. B. & Witelski, T. P. (2003) Coarsening dynamics of dewetting films. *Phys. Rev. E (3)*, **67**, 016302.

Gomba, J. & Homsy, G. (2009) Analytical solutions for partially wetting two-dimensional droplets. *Langmuir*, **25**, 5684–5691.

Honisch, C., Lin, T.-S., Heuer, A., Thiele, U. & Gurevich, S. V. (2015) Instabilities of layers of deposited molecules on chemically stripe patterned substrates: ridges versus drops. *Langmuir*, **31**, 10618–10631.

Hutchinson, A., Harley, C. & Momoniat, E. (2013) Numerical investigation of the steady state of a driven thin film equation. *J. Appl. Math.*, **2013**.

Kao, J. C. T., Golovin, A. A. & Davis, S. H. (2006) Rupture of thin films with resonant substrate patterning. *J. Colloid Interface Sci.*, **303**, 532–545.

Kargupta, K., Konnur, R. & Sharma, A. (2000) Instability and pattern formation in thin liquid films on chemically heterogeneous substrates. *Langmuir*, **16**, 10243–10253.

Kargupta, K. & Sharma, A. (2001) Templating of thin films induced by dewetting on patterned surfaces. *Phys. Rev. Lett.*, **86**, 4536.

Kargupta, K. & Sharma, A. (2002) Morphological self-organization by dewetting in thin films on chemically patterned substrates. *J. Chem. Phys.*, **116**, 3042–3051.

Kašpar, O., Zhang, H., Tokárová, V., Boysen, R. I., Suñé, G. R., Borrise, X., Perez-Murano, F., Hearn, M. T. & Nicolau, D. V. (2016) Confinement of water droplets on rectangular micro/nano-arrayed surfaces. *Lab Chip*, **16**, 2487–2493.

Kevorkian, J. & Cole, J. D. (1996) *Multiple Scale and Singular Perturbation Methods*. Applied Mathematical Sciences, vol. 114. New York: Springer.

Kooij, E. S., Jansen, H., Bliznyuk, O., Poelsema, B. & Zandvliet, H. J. (2012) Directional wetting on chemically patterned substrates. *Colloids Surf. A Physicochem. Eng. Asp.*, **413**, 328–333.

Laugesen, R. S. & Pugh, M. C. (2000a) Linear stability of steady states for thin film and Cahn–Hilliard type equations. *Arch. Rational Mech. Anal.*, **154**, 3–51.

Laugesen, R. S. & Pugh, M. C. (2000b) Properties of steady states for thin film equations. *European J. Appl. Math.*, **11**, 293–351.

Lenz, P. & Lipowsky, R. (1998) Morphological transitions of wetting layers on structured surfaces. *Phys. Rev. Lett.*, **80**, 1920.

Lenz, R. D. & Kumar, S. (2007) Competitive displacement of thin liquid films on chemically patterned substrates. *J. Fluid Mech.*, **571**, 33–57.

Liu, W. (2019) Dynamics and steady-states of thin film droplets on homogeneous and heterogeneous substrates. *Ph.D. Thesis*, Durham, North Carolina, USA: Duke University.

Lo, R. C. (2013) Application of microfluidics in chemical engineering. *Chem. Eng. Process Technol.*, **442**, 368–373.

Lubarda, V. A. & Talke, K. A. (2011) Analysis of the equilibrium droplet shape based on an ellipsoidal droplet model. *Langmuir*, **27**, 10705–10713.

Mac Intyre, J. R., Gomba, J. M. & Perazzo, C. A. (2016) New analytical solutions for static two-dimensional droplets under the effects of long-and short-range molecular forces. *J. Engrg. Math.*, **101**, 55–69.

Moosavi, A., Rauscher, M. & Dietrich, S. (2008) Motion of nanodroplets near chemical heterogeneities. *Langmuir*, **24**, 734–742.

Murdock, J. A. (1999) *Perturbations: Theory and Methods*. Classics in Applied Mathematics, vol. 27. Philadelphia, PA: Society for Industrial and Applied Mathematics (SIAM).

Myers, T. (1998) Thin films with high surface tension. *SIAM Rev.*, **40**, 441–462.

O'Brien, S. & Schwartz, L. (2002) Theory and modeling of thin film flows. *Encyclopedia of Surface and Colloid Science*, Marcel Dekker, New York, pp. 5283–5297.

Ockendon, J. R. & Ockendon, H. (1995) *Viscous Flow*. Cambridge: Cambridge University.

Oron, A. & Bankoff, S. G. (1999) Dewetting of a heated surface by an evaporating liquid film under conjoining/disjoining pressures. *J. Colloid Interface Sci.*, **218**, 152–166.

Oron, A. & Bankoff, S. G. (2001) Dynamics of a condensing liquid film under conjoining/disjoining pressures. *Phys. Fluids*, **13**, 1107–1117.

Oron, A., Davis, S. H. & Bankoff, S. G. (1997) Long-scale evolution of thin liquid films. *Rev. Modern Phys.*, **69**, 931.

Pahlavan, A. A., Cueto-Felgueroso, L., Hosoi, A., McKinley, G. & Juanes, R. (2018) Thin films in partial wetting: stability, dewetting and coarsening. *J. Fluid Mech.*, **845**, 642–681.

Perazzo, C. A., Mac Intyre, J. R. & Gomba, J. M. (2017) Analytical solutions for the profile of two-dimensional droplets with finite-length precursor films. *Phys. Rev. E (3)*, **96**, 063109.

Sakai, M., Yanagisawa, T., Nakajima, A., Kameshima, Y. & Okada, K. (2008) Effect of surface structure on the sustainability of an air layer on superhydrophobic coatings in a water-ethanol mixture. *Langmuir*, **25**, 13–16.

Schwartz, L. & Eley, R. (1998) Simulation of droplet motion on low-energy and heterogeneous surfaces. *J. Colloid Interface Sci.*, **202**, 173–188.

Son, Y., Kim, C., Yang, D. H. & Ahn, D. J. (2008) Spreading of an inkjet droplet on a solid surface with a controlled contact angle at low Weber and Reynolds numbers. *Langmuir*, **24**, 2900–2907.

Thiele, U., Brusch, L., Bestehorn, M. & Bar, M. (2003) Modelling thin-film dewetting on structured substrates and templates: bifurcation analysis and numerical simulations. *Eur. Phys. J. E*, **11**, 255–271.

Thiele, U., Velarde, M. G. & Neuffer, K. (2001) Dewetting: film rupture by nucleation in the spinodal regime. *Phys. Rev. Lett.*, **87**, 016104.

Wang, J., Zheng, Z., Li, H., Huck, W. & Sirringshaus, H. (2004) Polymer field effect transistors fabricated by dewetting. *Synth. Met.*, **146**, 287–290.

Whitesides, G. M. (2006) The origins and the future of microfluidics. *Nature*, **442**, 368.

Witelski, T. P. & Bowen, M. (2003) ADI schemes for higher-order nonlinear diffusion equations. *Appl. Numer. Math.*, **45**, 331–351.

Yuan, Y. & Lee, T. R. (2013) Contact angle and wetting properties. *Surface Science Techniques*. Berlin, Heidelberg: Springer, pp. 3–34.

Zope, M., Kargupta, K. & Sharma, A. (2001) Self-organized structures in thin liquid films on chemically heterogeneous substrates: effect of antagonistic short and long range interactions. *J. Chem. Phys.*, **114**, 7211–7221.

A. Proof of positivity and global existence of solutions

Here, we extend the proof given in Bertozzi *et al.* (2001) showing the global existence of positive solutions to (2.3a) from the homogeneous case ($A(x) \equiv 1$) to apply to heterogeneous substrates with positive $A(x)$ bounded from above.

THEOREM A.1 Consider the initial data for (2.3) satisfying $h_0(x) > 0$ with $h_0 \in H^1([0, L])$ and $E(h_0) < \infty$, then the solution $h(x, t)$ is positive for all $t > 0$.

Proof. We derive *a priori* pointwise upper and lower bounds for the solution. The energy E, as given by (2.5), is monotonically decreasing following (2.7). It follows that at any time $T > 0$,

$$\frac{1}{2}\int_0^L \left|\frac{\partial h}{\partial x}(T)\right|^2 \mathrm{d}x \leqslant \frac{1}{2}\int_0^L \left|\frac{\partial h_0}{\partial x}\right|^2 \mathrm{d}x + \int_0^L A(x)U(h_0)\,\mathrm{d}x - \int_0^L A(x)U(h(T))\,\mathrm{d}x. \tag{A.1}$$

Using that $A(x)$ is bounded and $-U(h)$ has an *a priori* upper bound independent of h (from (2.6), $U(h) \geqslant 1/6$ for all $h > 0$), implies that $\int |\partial_x h(x, T)|^2\,\mathrm{d}x$ is bounded. Hence, $h(x, T) \in H^1([0, L])$. Then, $h(x, T)$ has both *a priori* pointwise and $C^{0,1/2}$ upper bounds by the Sobolev embedding theorem.

Note that (A.1) along with the boundedness of $A(x)$ implies $\int_0^L U(h(x, T))\,\mathrm{d}x < C$. Suppose $h(x, T)$ attains its minimum $h_{\min}$ at $x = x_0$. By Holder continuity, $h(x) \leqslant h_{\min} + C_h|x - x_0|^{1/2}$. Therefore,

$$C > \int_0^L U(h(x, T))\,\mathrm{d}x \geqslant \int_0^L \left(\frac{\varepsilon^3}{3(h_{\min} + C_h|x - x_0|^{1/2})^3} - \frac{\varepsilon^2}{2h_{\min}^2}\right)\mathrm{d}x \geqslant \frac{C_2(\varepsilon, L)}{h_{\min}} + O(1). \tag{A.2}$$

Hence, the solution cannot go below a positive threshold for any $T > 0$. □